UNIVERSIDADE FEDERAL DE MINAS GERAIS

Escola de Engenharia

Programa de Pós-Graduação em Engenharia Metalúrgica, Materiais e de Minas

Alice Gameiro Leonel

DESENVOLVIMENTO DE PEROVSKITAS DO TIPO $LaBO_3$ (B = Fe, Co, Cu, E Fe+Cu) A PARTIR DOS MÉTODOS CITRATO E *NANOCASTING* PARA REMEDIAÇÃO AMBIENTAL UTILIZANDO PROCESSOS AVANÇADOS DE OXIDAÇÃO

Belo Horizonte

2024

Alice Gameiro Leonel

DEVELOPMENT OF $LaBO_3$ (B = Fe, Co, Cu, AND Fe+Cu) PEROVSKITE CATALYSTS FROM A CITRATE AND HARD-TEMPLATE-BASED NANOCASTING METHODS FOR WATER REMEDIATION THROUGH ADVANCED OXIDATION PROCESSES

Material presented to the Graduate Program in Metallurgical, Materials and Mining Engineering, School of Engineering, Federal University of Minas Gerais, as a requirement to obtain a Doctor's Degree in Materials Science and Engineering.
Concentration Area: Materials Science and Engineering

Advisor: Prof. Dr. Eduardo Henrique Nunes Martins
Co advisor: Dr. Himad Ahmed Alcamand

Belo Horizonte
2024

Leonel, Alice Gameiro.
L583d Development of $LaBO_3$ (B = Fe, Co, Cu, and Fe+Cu) perovskite catalysts from a citrate and hard-template-based nanocasting methods for water remediation through advanced oxidation processes [recurso eletrônico] / Alice Gameiro Leonel. - 2024.
1 recurso online (92 f.: il., color.): pdf.

Orientador: Eduardo Henrique Martins Nunes.
Coorientador: Himad Ahmed Alcamand.

Tese (doutorado) - Universidade Federal de Minas Gerais, Escola de Engenharia.

Bibliografia: f. 84-92.
Exigências do sistema: Adobe Acrobat Reader.

1. Materiais - Teses. 2. Ciência dos materiais - Teses. 3. Catalisadores - Teses. 4. Águas residuais - Tratamento - Teses. 5. Lantânio - Teses. I. Nunes, Eduardo Henrique Martins. II. Alcamand, Himad Ahmed. III. Universidade Federal de Minas Gerais. Escola de Engenharia. IV. Título.

CDU: 620(043)

Ficha catalográfica elaborada pelo bibliotecário Reginaldo César Vital dos Santos CRB/6 2165
Biblioteca Prof. Mário Werneck, Escola de Engenharia da UFMG

UNIVERSIDADE FEDERAL DE MINAS GERAIS
ENGENHARIA - COLEGIADO DE PÓS-GRADUAÇÃO EM ENGENHARIA METALÚRGICA MATERIAIS E DE MINAS - SECRETARIA

ATA DE DEFESA DE TESE

Às 13:30h do dia 21 (vinte e um) de novembro de 2024, na sala 2240 do Bloco da Escola de Engenharia da UFMG, realizou-se a sessão pública da defesa de tese de Doutorado da aluna **ALICE GAMEIRO LEONEL**, para a obtenção do grau de Doutora em Engenharia Metalúrgica, Materiais e de Minas, na área de concentração de Ciência e Engenharia de Materiais. O presidente da sessão, Prof. Eduardo Henrique Martins Nunes - Dr. (UFMG), orientador da aluna, apresentou a comissão examinadora, composta pelos seguintes membros: **Manuel Houmard - Dr. (UFMG), Hugo Guimarães Palhares - Dr. (UFMG), Daniel Cristian Ferreira Soares - Dr. (UNIFEI), Taiane Guedes Fonseca de Souza - Dra. (CEFET/MG) e Mariana Govoni Brondi Wolf - Dra. (Embrapa)**. Na sequência, a candidata realizou a apresentação de sua Tese de Doutorado, intitulada "**Development of Mesoporous $LaBO_3$ (b = Fe, Cu, Co, And Fe+Cu) Perovskite Catalysts from a Hard-template-based Nanocasting Method for Water Remediation Through Advanced Oxidation Processes**". Após a apresentação, os examinadores procederam à arguição da candidata. Concluída essa etapa, a comissão reuniu-se em caráter reservado, sem a presença da candidata e do público, e decidiu por **APROVAR** a Tese de Doutorado. O resultado final foi comunicado publicamente à candidato(a) pelo presidente da sessão. Não havendo mais nada a tratar, o presidente encerrou a sessão e lavrou a presente ata, que, após lida, foi assinada pelos membros da comissão examinadora e pelo coordenador do Programa.

Belo Horizonte, 21 de novembro de 2024.

Assinatura dos membros da banca examinadora:

Documento assinado eletronicamente por **Daniel Cristian Ferreira Soares, Usuário Externo**, em 26/11/2024, às 07:50, conforme horário oficial de Brasília, com fundamento no art. 5º do Decreto nº 10.543, de 13 de novembro de 2020.

Documento assinado eletronicamente por **Mariana Govoni Brondi Wolf, Usuária Externa**, em 26/11/2024, às 20:15, conforme horário oficial de Brasília, com fundamento no art. 5º do Decreto nº 10.543, de 13 de novembro de 2020.

Documento assinado eletronicamente por **Hugo Guimaraes Palhares, Usuário Externo**, em 28/11/2024, às 19:54, conforme horário oficial de Brasília, com fundamento no art. 5º do Decreto nº 10.543, de 13 de novembro de 2020.

Documento assinado eletronicamente por **Taiane Guedes Fonseca de Souza, Usuário Externo**, em 02/12/2024, às 22:40, conforme horário oficial de Brasília, com fundamento no art. 5º do Decreto nº 10.543, de 13 de novembro de 2020.

Documento assinado eletronicamente por **Eduardo Henrique Martins Nunes, Professor do Magistério Superior**, em 03/12/2024, às 17:56, conforme horário oficial de Brasília, com fundamento no art. 5º do Decreto nº 10.543, de 13 de novembro de 2020.

Documento assinado eletronicamente por **Manuel Noel Paul Georges Houmard, Professor(a)**, em 22/01/2025, às 14:01, conforme horário oficial de Brasília, com fundamento no art. 5º do Decreto nº 10.543, de 13 de novembro de 2020.

Documento assinado eletronicamente por **Daniel Majuste, Professor do Magistério Superior**, em 22/01/2025, às 16:34, conforme horário oficial de Brasília, com fundamento no art. 5º do Decreto nº 10.543, de 13 de novembro de 2020.

A autenticidade deste documento pode ser conferida no site https://sei.ufmg.br/sei/controlador_externo.php?acao=documento_conferir&id_orgao_acesso_externo=0, informando o código verificador **3732501** e o código CRC **95C30FD9**.

Ao meu orientador, Eduardo Henrique Martins Nunes, pela confiança na construção deste trabalho e pelo absoluto incentivo ao longo dessa duradoura e desafiante jornada.

AGRADECIMENTOS

E finalmente é chegada a hora de encerrar o ciclo. Um projeto que chegou ao fim. Um projeto que nos primeiros anos parecia não estar dando certo, apesar de todo o meu comprometimento, esforço, insistência e desconforto. Que depois de muita coragem para enfrentar uma difícil mudança, sem ter a certeza de que direção seguir, mas sabendo para onde não mais voltar, deu muito certo!! Agora compartilho o mais profundo sentimento de GRATIDÃO pelas oportunidades que tive, pelas escolhas que fiz e pelas pessoas que encontrei ao longo do caminho. A essas pessoas meus sinceros agradecimentos:

Ao meu orientador Eduardo por ter me convidado a fazer parte do seu grupo de pesquisa, pela confiança que depositou em mim e no meu trabalho, por todo o conhecimento compartilhado, dedicação e exemplo de profissional. Esse doutorado não existiria se não fosse você.

Ao meu noivo Herbert por todo o apoio, carinho e atenção incondicionais. Por sempre me incentivar e confiar em minhas capacidades mais do que eu mesma.

À minha irmã querida Letícia, pela presença constante, mesmo que fisicamente ausente, pelas trocas de experiências e por ser um porto seguro para mim.

Aos meus pais Carlos e Rosângela por todos os ensinamentos, valores transmitidos e suporte ao longo da minha vida. Vocês são responsáveis pela pessoa que me tornei.

À Camilla Gordiana e Ana Carolina Sarquis por cuidarem de mim com tanta dedicação, empatia sabedoria e respeito frente as minhas dificuldades.

A todos os colegas do Laboratório de Biomateriais pelo acolhimento, amizade, convivência diária, troca de conhecimento e momentos de descontração. Ao Himad pelo suporte inicial quando ainda descobria o universo das perovskitas. À Patricia Rodrigues, que de um modo especial, também faz parte do laboratório e sempre esteve à disposição para ajudar.

As queridas Nádia, Isadora, Marina, Daísa e Thaiara, amizades da UFMG para a vida. Obrigada por tudo e por tanto! Os dias na UFMG são melhores por causa da presença de vocês.

Aos professores Rodrigo Oréfice, Andréia Bicalho, Virgínia Ciminelli e Sônia Rocha por disponibilizarem a infraestrutura de seus laboratórios e recursos para a realização de ensaios. Aos técnicos Ricardo Oliveira, Fernando Souza, Claudia Caldeira e André Santos pelo auxílio na realização de cada ensaio. Ao CTNano e em especial ao Prof. Manuel Houmard por disponibilizarem a infraestrutura do centro de pesquisa para análises de BET. Ao Centro de Microscopia pela realização dos ensaios de microscopia de transmissão.

Ao Programa de Pós-Graduação em Engenharia Metalúrgica, Materiais e de Minas (PPGEM) pela oportunidade de especialização e, em especial, aos funcionários Cida, Kelly e Diego que, gentilmente, sempre estiveram à disposição para nos atender.

Aos órgãos de fomento CAPES, CNPq e FAPEMIG pelo auxílio financeiro e incentivo à pesquisa.

“Feliz aquele que transfere o que sabe e aprende o que ensina”.

(Cora Coralina)

ABSTRACT

The rapid growth of industrialization, combined with a growing population, has created an unprecedented demand for safe, reliable, and cost-effective water supply, which has become one of the greatest challenges of the 21st century. In particular, the application of La-based perovskites for environmental remediation has currently received remarkable attention due to their outstanding thermal stability and versatility, which favor their use in a wide range of advanced applications, including catalysis. However, they have an inherently low specific surface area, which can typically negatively affect their performance in surface-related processes. In this sense, the development of mesoporous perovskites for water treatment has attracted attention as a powerful catalyst. In the first part of this study, we synthesized $LaBO_3$ perovskites by changing the transition metal present at the B-site, including Cu, Fe, Co, and a combination of Cu and Fe. These materials were prepared using the citrate process, with special call to environmental safety issues, avoiding the use of organic solvents. The catalytic behavior of the prepared perovskites was evaluated using two different advanced oxidation processes for the degradation of methylene blue: Fenton-like and sulfate radical-based reactions. The catalyst-to-contaminant dosing ratio, solution pH, type of oxidant (either hydrogen peroxide or potassium peroxymonosulfate), and their respective concentrations were also evaluated. We observed that the co-doping of La-based perovskites with Cu and Fe resulted in samples with improved catalytic performance, reaching a rate constant (k_{app}) as high as 0.25 min^{-1} despite their low surface area (5.9 $m^2.g^{-1}$). This improved catalytic behavior was attributed to a synergy of factors, including oxygen vacancy formation and redox properties. In the second part of this study, we synthesized mesoporous $La(Cu+Fe)O_3$ perovskites through the nanocasting method using the SBA-16 as a hard template. The influence of mesoporosity on the structural and catalytic properties of these materials was investigated. The mesoporous structure was found to increase the specific surface area of the nanocast perovskites by a factor of ten. The catalytic performance of this specific perovskite was, for the first time in the literature, evaluated for the degradation of doxorubicin, a widely used chemotherapeutic drug, through sulfate radical-based reactions. A significant improvement in catalytic performance was demonstrated, suggesting that efficient catalysts for environmental remediation can be obtained by optimizing the mesoporosity of perovskite materials.

Keywords: lanthanum-based perovskites; B-site substitution; SBA-16 mesoporous silica; wastewater treatment; Fenton-like reactions; sulfate radical-based reactions.

RESUMO

O rápido crescimento industrial, combinado com o aumento da população, têm ocasionado uma demanda sem precedentes pelo fornecimento de água de forma segura, confiável e econômica, o que se tornou um dos maiores desafios do século XXI. Em particular, a aplicação de perovskitas à base de La para remediação ambiental tem recebido atenção especial devido à sua excelente estabilidade térmica e versatilidade, que favorecem sua utilização em processos catalíticos. No entanto, esses materiais exibem uma baixa área superficial específica, inerente de seus processos de síntese em elevadas temperaturas, que pode afetar negativamente seu desempenho catalítico. Neste sentido, o desenvolvimento de perovskitas mesoporosas para tratamento de água tem atraído bastante atenção. Na primeira parte deste trabalho, foram produzidas perovskitas do tipo $LaBO_3$ alterando o metal de transição presente no sítio B por Cu, Fe, Co e uma combinação de Cu e Fe. Esses materiais foram produzidos pelo método convencional citrato, com especial atenção à questão ambiental, evitando o uso de solventes orgânicos. O comportamento catalítico das perovskitas foi avaliado utilizando reações do tipo Fenton e reações baseadas em geração de radical sulfato para a degradação do corante azul de metileno. A razão molar catalisador/poluente, pH da solução, tipo de oxidante (H_2O_2 ou PMS) e sua concentração também foram avaliados. Foi observado que a co-dopagem das perovskitas com Cu e Fe resultou em amostras com melhor desempenho catalítico, atingindo uma taxa de reação (k_{app}) de 0,25 min^{-1}, apesar de sua baixa área superficial específica (5,9 $m^2.g^{-1}$). Esta melhor atividade catalítica foi atribuída a uma sinergia de fatores, incluindo a formação de lacunas de oxigênio na rede cristalina e propriedades redox dos elementos constituintes. Na segunda parte deste trabalho, foram produzidas perovskitas mesoporosas do tipo $La(Cu+Fe)O_3$ por meio do método *nanocasting* utilizando a sílica mesoporosa SBA-16 como *template*. A influência da mesoporosidade nas propriedades estruturais e catalíticas destes materiais foi investigada. Verificou-se que a estrutura mesoporosa aumentou em dez vezes a área superficial específica dessas perovskitas. Pela primeira vez reportado na literatura, o desempenho catalítico foi avaliado utilizando reações baseadas em geração de radicais sulfato para a degradação da doxorrubicina, agente quimioterápico amplamente utilizado. O significativo aumento no desempenho catalítico sugere que catalisadores eficientes para tratamento de água podem ser obtidos otimizando-se a mesoporosidade do material.

Palavras-chave: perovskitas à base de lantânio; substituição no sítio B; sílica mesoporosa SBA-16; tratamento de águas residuais; reações do tipo Fenton; reações baseadas em radicais sulfato.

SUMMARY OF FIGURES

SUMMARY OF TABLES

LIST OF ABBREVIATIONS AND NOTATIONS

AOPs	Advanced oxidation processes
ATR	Attenuated Total Reflectance
CA	Citric acid
DI	Deionized water
DOX	Doxorubicin
DRS	UV-Diffuse Reflectance Spectroscopy
EDS	Energy Dispersive X-ray Spectroscopy
EDTA	Ethylenediaminetetraacetic acid
ENM	Engineered nanomaterial
EPR	Electronic Paramagnetic Resonance
EtOH	Ethanol
FTIR	Fourier Transformed Infrared spectroscopy
ICDD	International Center for Diffraction Data
k_{app}	Reaction constant rate
LH	Langmuir-Hinshelwood
LFO	$LaFeO_3$
LCuO	$LaCuO_3$
LCoO	$LaCoO_3$
LCuFO	$LaCu_{0.1}Fe_{0.9}O_3$
LCuFO_SBA-16	Mesoporous LCuFO
MB	Methylene blue
MTT	Cell viability test
NO-MS	Non-ordered mesoporous silica
O_{ads}	Adsorbed oxygen
O_{lat}	Lattice oxygen
O_v	Oxygen vacancy
PMS	Peroxymonosulfate
PS	Persulfate
PZC	Point of Zero Charge
ROS	Reactive oxygen species
RT	Room temperature
SAED	Selected-area Electron Diffraction

SBA-16	Ordered mesoporous silica
SSA	Specific surface area
TEM	Transmission Electron Microscopy
TEOS	Tetraethyl orthosilicate
TOC	Total Organic Carbon
UV-vis	Ultraviolet-visible Spectroscopy
XPS	X-ray Photoelectron Spectroscopy
XRD	X-ray Diffraction

SUMMARY

1. INTRODUCTION

One of the greatest challenges facing global society in the twenty-first century is providing water in a safe, reliable, and cost-effective manner. Rapid industrialization, population growth, and changing lifestyles have led to an unprecedented increase in production combined with inappropriate disposal of hazardous industrial by-products into water systems, such as organic dyes, heavy metals, pesticides, and pharmaceutical residues. In this scenario, environmental remediation has become an urgent need to maintain ecological stability and public health (ALVAREZ et al., 2018; KALITA; BARUAH, 2020; LU; ASTRUC, 2020).

Although various conventional technologies have been used for water treatment, including chemical precipitation, flotation, gravity separation, solvent extraction, ion exchange, and membrane filtration (SANTHOSH et al., 2016; ZITO; SHIPLEY, 2015), most of these methods have several drawbacks, such as time consumption, partial effectiveness, and high cost (CORSI et al., 2018).

Over the past few decades, new opportunities in nanotechnology have stimulated research exploring the use of engineered nanomaterials in adsorption and advanced oxidation processes (AOPs) (HODGES; CATES; KIM, 2018). The former uses nanomaterials as sorbents to improve removal efficiency, while the latter uses them as catalysts to mineralize or convert contaminants into inert products. In many applications, however, a combination of the two processes is observed (XU et al., 2012).

Adsorption is considered one of the most practical options because of its lower initial cost, simple design, and straightforward operation. This method is highly dependent on the nature and magnitude of the adsorbent-adsorbate interactions. It is therefore primarily influenced by factors such as the chemical structure and specific surface area of the adsorbent, effluent pH, pollutant concentration, and contact time. Considerable efforts have been made to obtain inexpensive and effective adsorbents. However, due to the complex chemical structures of recalcitrant contaminants, their removal by adsorption may not be fully efficient. Additionally, the process involves transferring the contaminant from one phase to another, which can lead to the generation of waste (JUENGCHAREONPOON; WANICHPONGPAN; BOONAMNUAYVITAYA, 2021).

Alternatively, AOPs are effective in wastewater remediation through the *in situ* generation of highly reactive radicals with strong oxidative capabilities, providing an innovative solution for the non-specific degradation of most recalcitrant contaminants into less toxic species (FERROUDJ et al., 2017; WANG et al., 2016). The superior performance of catalytic nanomaterials is mainly due to their high surface area and consequently high chemical reactivity (CORSI et al., 2018; KALITA; BARUAH, 2020). Among AOPs, Fenton and Fenton-like heterogeneous oxidation are promising alternatives for wastewater treatment. Traditionally, in these catalytic reactions, iron species (Fe^{2+} and Fe^{3+}) are reversibly oxidized and reduced in the presence of hydrogen peroxide (H_2O_2) to generate OH radicals ($HO^{\bullet}$), which undergo a sequence of chemical transformations, leading to different oxidation products (BABUPONNUSAMI; MUTHUKUMAR, 2014; MIRZAEI et al., 2017). Other multi-redox metal transition ions such as Cr, Co, Cu, Ni, and Mn can also degrade H_2O_2 to free radicals via conventional Fenton-like pathways (CARRASCO-DÍAZ et al., 2016). Another promising alternative AOP is the sulfate radical-based reactions because the main oxidant (peroxymonosulfate-PMS) often used to generate these radicals is considered to be less expensive, more stable compared to H_2O_2, has a similar or even stronger oxidation potential than $HO^{\bullet}$ ($E^0 = 2.5\text{-}3.1$ V *vs.* 2.8 V), a wide operating pH range (from 2 to 8), and solubility/stability in water (HODGES; CATES; KIM, 2018; XIAO et al., 2020).

Although iron oxide nanomaterials have been extensively studied in catalytic processes via Fenton and Fenton-like reactions, perovskites have emerged as a promising alternative in recent years. Perovskites are mixed-metal oxides with a general formula ABO_3, where A represents an alkali, alkaline earth, or rare-earth metal, and B is a transition metal from the 3d, 4d, or 5d configuration. This material attracts much interest in environmental catalysis due to its high thermal stability, oxidation activity, and versatility. The outstanding structural flexibility of perovskites is due to their versatile chemical composition, which results from the diversity of metal ions that can fit into both A and B sites without destroying the crystal structure but altering their stoichiometry and defect concentration. Perovskites containing lanthanum at the A-site are often used as efficient heterogeneous catalysts, although it has been reported that the A-site cation has no catalytic activity. However, it will affect the chemical state of the B-site and the generation of oxygen vacancies, which can improve the catalytic performance (DEL ÁLAMO et al., 2020; LIN et al., 2022; ROJAS-CERVANTES; CASTILLEJOS, 2019).

Developing perovskites with high specific surface area (SSA) is crucial for improving adsorption and catalysis. Since the SSA of perovskites is typically low, limiting the interaction between the pollutant and the active sites, several strategies have been developed to increase their surface area. One such approach involves the use of silica templates that create porosity in the perovskite catalysts, thereby overcoming the limitation of low SSA (LI et al., 2023a; ROJAS-CERVANTES; CASTILLEJOS, 2019).

In this study, we present the synthesis and characterization of various La-based perovskite catalysts with potential applications in advanced oxidation processes for water remediation. In the first part of the study, we synthesized $LaBO_3$ perovskites by varying the transition metal at the B-site, including Cu, Fe, Co, and a combination of Cu and Fe. These materials were prepared using the citrate method, with a focus on environmental safety by avoiding the use of organic solvents. The catalytic behavior of the prepared perovskites was assessed using two different advanced oxidation processes for the degradation of methylene blue (MB): Fenton-like and sulfate radical-based reactions. We also evaluated the catalyst-to-contaminant dosing ratio, solution pH, oxidant type (either hydrogen peroxide or potassium peroxymonosulfate), and their respective concentrations. In the second part of the study, we synthesized mesoporous $La(Cu+Fe)O_3$ perovskites using the nanocasting method, with SBA-16 as a hard template. The impact of mesoporosity on the structural and catalytic properties of these materials was explored. For the first time in the literature, the catalytic performance of this specific perovskite was evaluated for the degradation of doxorubicin (DOX), a widely used chemotherapeutic drug, via sulfate radical-based reactions.

INTRODUÇÃO

Um dos maiores desafios do século XXI enfrentado pela sociedade global é fornecimento de água de forma segura, confiável e de baixo custo. O rápido crescimento da industrialização, associado ao aumento populacional e as mudanças no estilo de vida das pessoas levaram a um aumento sem precedentes na produção resíduos e do descarte inadequado de subprodutos industriais tóxicos em sistemas de água, como por exemplo, corantes orgânicos, metais pesados, pesticidas e produtos farmacêuticos. Em vista desse cenário, a remediação ambiental tornou-se uma necessidade a preservação do meio ambiente e da saúde pública (ALVAREZ et al., 2018; KALITA; BARUAH, 2020; LU; ASTRUC, 2020).

Embora uma variedade de tecnologias convencionais tenham sido utilizadas para o tratamento de água, incluindo precipitação química, flotação, separação por gravidade, extração por solvente, troca iônica e filtração por membrana (SANTHOSH et al., 2016; ZITO; SHIPLEY, 2015), a maioria desses métodos apresentam limitações, como consumo de tempo, eficácia parcial e altos custos (CORSI et al., 2018).

Nas últimas décadas, novas oportunidades em nanotecnologia estimularam pesquisas explorando o uso de nanomateriais em adsorção e processos de oxidação avançada (AOPs) (HODGES; CATES; KIM, 2018). Enquanto o primeiro utiliza nanomateriais como um adsorvente para melhorar a eficiência de remoção de contaminantes, o segundo faz seu uso como um catalisador para mineralizar ou converter esses contaminantes em produtos inertes. No entanto, em muitas aplicações, observa-se a combinação de ambos os processos (XU et al., 2012).

A adsorção é considerada uma das opções mais práticas, pois possui um custo operacional inicial menor, e um simples design. Este método é altamente dependente da natureza das interações adsorvente-adsorbato e da magnitude dessas interações. Assim, é influenciado principalmente por fatores como a estrutura química e área superficial do adsorvente, pH do efluente, concentração do poluente e tempo de contato entre as espécies envolvidas no processo. Esforços consideráveis têm sido feitos para a obtenção de adsorventes eficazes e de baixo custo. No entanto, devido às complexas estruturas químicas dos contaminantes, sua remoção por adsorção pode não ser completamente eficiente. Além disso, o processo implica em deslocar a substância tóxica de uma fase para outra, não transformando-a em subprodutos

menos tóxicos (JUENGCHAREONPOON; WANICHPONGPAN; BOONAMNUAYVITAYA, 2021).

Alternativamente, os AOP´s demonstraram ser eficazes para o tratamento de águas residuais por meio da geração *in situ* de radicais extremamente reativos, que têm uma forte capacidade de oxidação e representam uma solução inovadora para degradar de forma não específica a maioria dos contaminantes em espécies menos tóxicas (FERROUDJ et al., 2017; WANG et al., 2016). O melhor desempenho dos nanomateriais catalíticos pode ser atribuído principalmente à elevada área superficial e, consequentemente, à alta reatividade química (CORSI et al., 2018; KALITA; BARUAH, 2020). Dentre os AOP´s existentes, as reações Fenton e do tipo Fenton constituem uma ótima alternativa para o tratamento de efluentes. Tradicionalmente, nessas reações catalíticas, espécies de ferro (Fe^{2+} e Fe^{3+}) são reversivelmente oxidadas e reduzidas na presença de peróxido de hidrogênio (H_2O_2) para gerar radicais hidroxila ($HO^{\bullet}$), que passam por uma sequência de transformações químicas, produzindo diferentes sub-produtos de reação (BABUPONNUSAMI; MUTHUKUMAR, 2014; MIRZAEI et al., 2017). Outros íons de metais de transição com múltiplos estados redox, como Cr, Co, Cu, Ni e Mn também podem decompor H_2O_2 em radicais livres por meio de reações do tipo Fenton (CARRASCO-DÍAZ et al., 2016). Uma outra alternativa promissora de AOP´s são as reações baseadas em radicais sulfato, devido ao fato do principal oxidante (peroximonossulfato-PMS) frequentemente utilizado para a geração desses radicais ser considerado mais economicamente viável, mais estável em comparação ao H_2O_2, possuir potencial de oxidação semelhante ou até superior ao $HO^{\bullet}$ (E^0=2,5-3,1 V *vs*. 1,8 V), ampla faixa de pH operacional (de 2 a 8) e solubilidade/estabilidade em água (HODGES; CATES; KIM, 2018; XIAO et al., 2020).

Embora os nanomateriais de óxido de ferro tenham sido extensivamente investigados em processos catalíticos por meio de reações de Fenton, nos últimos anos a utilização de perovskitas surgiu como uma alternativa promissora. As perovskitas são materiais pertencente à classe óxidos metálicos mistos com fórmula geral do tipo ABO_3, onde A representa um metal alcalino, alcalino-terroso ou metal de terras raras, enquanto B representa um metal de transição. Este material está atraindo muito interesse como catalisador devido à sua alta estabilidade térmica, atividade de oxidação e versatilidade. Sua excelente flexibilidade estrutural decorre de sua composição química versátil, originada pela diversidade de íons metálicos que podem ocupar sítios A e B sem alterar a estrutura cristalina, mas modificando

sua estequiometria e concentração de defeitos. Perovskitas à base de lantânio no sítio A são frequentemente utilizadas como catalisadores heterogêneos eficientes, embora tenha sido relatado que o cátion presente no sítio A não apresenta atividade catalítica. No entanto, a substituição parcial do La pode influenciar no número de oxidação do metal de transição do sítio B e na geração de vacâncias de oxigênio na estrutura cristalina, o que pode melhorar o desempenho catalítico (DEL ÁLAMO et al., 2020; LIN et al., 2022; ROJAS-CERVANTES; CASTILLEJOS, 2019).

O desenvolvimento de perovskitas com elevada área superficial específica (SSA) é essencial para os processos de adsorção e catálise. Considerando que a área de superfície das perovskitas é baixa, ou seja, a interação entre o poluente e os sítios ativos é restrita, algumas estratégias foram desenvolvidas para se obter perovskitas com maior área de superfície, incluindo a utilização de sílica mesoporosa na síntese das mesmas (LI et al., 2023a; ROJAS-CERVANTES; CASTILLEJOS, 2019).

Neste estudo, apresentamos a síntese e a caracterização de catalisadores de perovskita à base de La com potenciais aplicações em processos avançados de oxidação para tratamento de água. Na primeira parte do estudo, sintetizamos perovskitas do tipo $LaBO_3$ variando o metal de transição no sítio B, incluindo Cu, Fe, Co e uma combinação de Cu e Fe. Esses materiais foram sintetizados por meio do método citrato, com foco em sustentabilidade ambiental, evitando o uso de solventes orgânicos. O comportamento catalítico dessas perovskitas foi avaliado utilizando dois processos diferentes de oxidação avançada para a degradação do corante azul de metileno (MB): reações do tipo Fenton e reações baseadas na geração de radical sulfato. Também avaliamos a razão molar catalisador/contaminante, o pH da solução, o tipo de oxidante (peróxido de hidrogênio ou peroximonossulfato de potássio) e suas respectivas concentrações. Na segunda parte do estudo, sintetizamos perovskitas mesoporosas $La(Cu+Fe)O_3$ por meio do método *nanocasting*, utilizando a sílica mesoporosa SBA-16 como um molde rígido. A influência da mesoporosidade nas propriedades estruturais e catalíticas desses materiais foi avaliada. Pela primeira vez na literatura, o desempenho catalítico dessa perovskita foi avaliado para a degradação da doxorrubicina (DOX), um fármaco quimioterápico amplamente utilizado, por meio de reações baseadas na geração de radical sulfato.

2. OBJECTIVES

2.1. General objective

The present study aims to develop a mesoporous perovskite matrix based on the SBA-16 nanocasting approach with potential for application in wastewater treatment.

2.2. Specific objectives

- Synthesize through the citrate route and characterize the $LaBO_3$ (B = Fe, Cu, Co, or Cu+Fe) perovskites in terms of their morphological, structural, and physicochemical properties;
- Investigate the influence of the transition metal ion (Cu^{2+}, Co^{2+}, or Fe^{3+}) present at the B-site on the morphological, structural, physicochemical properties, and catalytic behavior of the obtained samples;
- Synthesize and characterize the SBA-16 and NO_MS mesoporous silica in terms of their morphological, structural, and physicochemical properties;
- Synthesize through the nanocasting approach and characterize the mesoporous $La(Cu+Fe)O_3$ perovskites in terms of their morphological, structural, and physicochemical properties;
- Study the influence of the mesoporous structure on the adsorption and catalytic properties of the perovskite samples;
- Evaluate the catalytic activity of $LaBO_3$ and mesoporous $LaBO_3$ samples *via* the degradation of methylene blue (MB) through Fenton-like reactions and sulfate radicals-based reactions;
- Examine the influence of catalysts/pollutant loading ratio, initial pH solution, type, and concentration of oxidant (H_2O_2 or potassium monopersulfate – PMS) on the adsorption and catalytic properties of perovskites;
- Evaluate the catalytic activity of mesoporous $LaBO_3$ samples *via* the degradation of doxorubicin (DOX) through sulfate radicals-based reactions.

3. LITERATURE REVIEW

3.1. Perovskites

The term perovskite was first applied to the calcium titanate mineral ($CaTiO_3$), the first member of this structural family to be identified, and subsequently extended to materials with the general formula ABX_3. Typically, the A-site represents an alkali, alkaline earth, or lanthanide cation, while the B-site corresponds to 3d, 4d, or 5d transition metal ions. The classification of perovskites as oxides or halides depends on the nature of the anion X. When X is an oxygen atom, the perovskite is considered an oxide; conversely, when X is a halogen atom, the perovskite is classified as a halide (HWANG et al., 2017; MAMBA et al., 2022).

In terms of unit cell structure, ideal ABO_3 perovskites exhibit a cubic arrangement, where BO_6 octahedra share corners, and the larger A cation ($r_A > r_B$) is coordinated to the dodecahedral interstices, as shown in Fig. 3.1a. In reality, however, most ABO_3 cubic structures are distorted to some extent because a variety of elements from the periodic table (Fig. 3.1b) with different sizes and valence states can occupy the A and B sites. This leads to significant compositional flexibility and, consequently, tunable physical and chemical properties. The discrepancy in cation size can lead not only to lattice distortions, but also to the formation of alternative perovskite structures, including hexagonal, orthorhombic, rhombohedral, or non-perovskite structures. Therefore, it is essential to predict the stability of perovskites based on their constituents (BARTEL et al., 2019; MAMBA et al., 2022; VOORHOEVE et al., 1977).

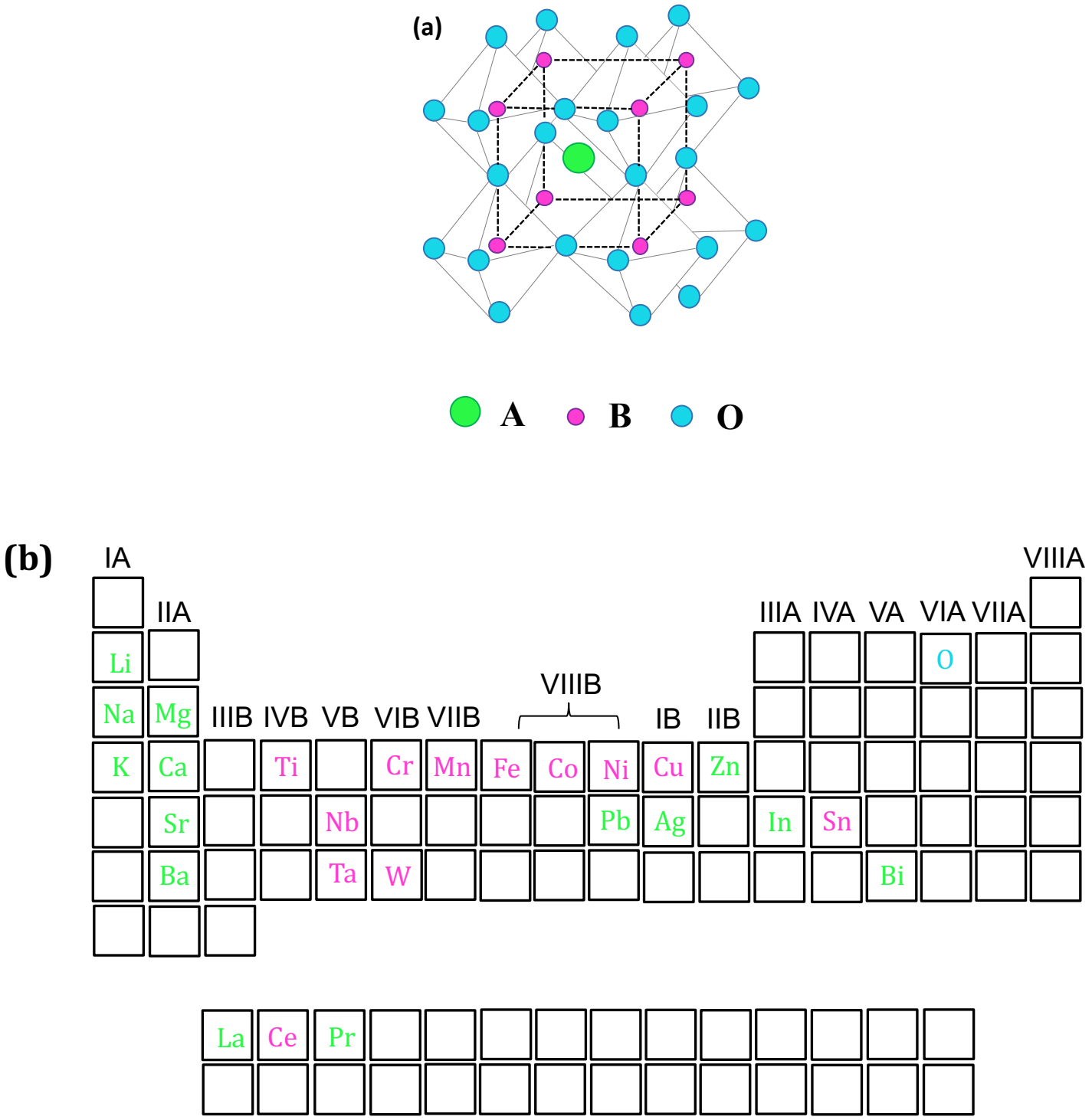

Figure 3.1 – (a) Schematic representation of the cubic ABO_3 perovskite unit cell and (b) representation of the elements that can occupy A and B-sites in mixed-oxide perovskites. Adapted from (PARWAIZ; KHAN, 2024).

3.1.1. Formation and structural stability of mixed-oxide perovskites

Among the many factors that can affect the stability of perovskites, crystalline structure transition is an important one. Complex oxides, such as ABO_3 perovskites, can accommodate different crystal structures depending on the size and interaction of the A cation and the corner-sharing BO_6 octahedra. For an ideal cubic ABO_3 structure, the A-O and B-O bond lengths are comparable; however, in the presence of lattice distortions, the B-O bond length and the B-O-B angle change, which could lead to the structural evolution of the cubic phase into octahedral, orthogonal, rhombohedral, tetragonal, monoclinic, and triclinic phases. The empirical index used to predict which structure will be preferentially formed is the Goldschmidt tolerance factor (t), as described in Eq. 3.1. (ATEIA; HASSAN; ABDELMAKSOUD, 2021; MAMBA et al., 2022).

$$t = \frac{r_A + r_O}{\sqrt{2}(r_B + r_O)} \tag{3.1}$$

where r_A is the radius of the A cation, r_B is the radius of the B cation, and r_O is the radius of the oxygen.

Ideally, a perfect cubic structure has a t value = 1, which means that the A cation fits perfectly into the BO_3 cavities. However, in general, materials with a tolerance factor in the range of 0.9−1.0 have an ideal cubic structure. A tolerance factor of 0.71-0.9 results in a distorted perovskite structure with a tilted octahedron. Meanwhile, a t value below 0.71 indicates that the A cation is too small to fit into the BO_6 cavities, and a t value above 1.0 indicates that the A cation is too large, which could lead to non-perovskite structures (KUMAR; KUMAR; KRISHNAN, 2020; MAMBA et al., 2022).

Another important parameter for predicting the stability of the cubic perovskite structure is the octahedral factor (μ) described by Eq. 3.2. In particular, it assesses the ability of the B site cation to occupy the octahedral cavity and be hexacoordinated to the O anions (KUMAR; KUMAR; KRISHNAN, 2020). Again, a perfect cubic structure will have μ close to 1.

$$\mu = \frac{r_B}{r_O} \tag{3.2}$$

3.1.2. Structural and physicochemical properties of $LaFeO_3$ (LFO) perovskites

Lanthanum ferrite is a typical perovskite that has attracted attention in many applications, including fuels and solar cells, sensors, light-emitting diodes, catalytic degradation of pollutants, water splitting, and electrochemical reduction of CO_2 (BACHA et al., 2023; LEONEL et al., 2024; WEI et al., 2022; ZHAO et al., 2024).

La is an environmentally friendly rare earth element with a large ionic radius (1.06 Å), which gives La-based perovskites high structural stability. $LaFeO_3$ exhibits an orthorhombic crystal structure at room temperature with the *Pbnm* space group, although its Goldschmidt tolerance factor (t = 0.954) indicates an idealized cubic structure formation. It can be related to the strong covalent bond between La and O species, which distorts the structure to optimize the orbital overlap, and the La-Fe coupled pair, which induces distortion in the FeO_6 octahedra. All these structural distortions are responsible for changing the electronic, optical, and magnetic properties, band structure, and charge separation ability (BACHA et al., 2023; MAMBA et al., 2022; PIDBURTNYI et al., 2021).

From a catalytic point of view, the high structural, chemical, and thermal stability of $LaFeO_3$ allows the use of the catalyst even under harsh reaction conditions, which can be favorable to reducing the loss of activity and consequently extend the life of the catalyst. Due to the high availability and low price of iron species, ferrites are more interesting than precious metals for this application. In addition, the presence of two stable valence states of iron (Fe^{2+} and Fe^{3+}) is critical for good oxidation activity (KUCHARCZYK et al., 2020; ROYER et al., 2014). However, this activity can be improved by cation substitution at the A and B sites. The following sections describe some effects of substitutions at the A and B sites of perovskites based on research results.

3.1.3. Influence of the cation present in A-sites on the properties of perovskites

As mentioned above, one of the major advantages of perovskite is its ability to accommodate a wide range of cations while maintaining structural stability. Cationic substitution has been extensively studied to improve the catalytic performance of perovskites in various advanced oxidation processes (BACHA et al., 2023; CHEN et al., 2024).

Concerning the A-site cation, it generally does not act directly as an active site in catalysis as long as it has a single valence state in the structure. However, variations in this cation can affect the coordination environment of the B sites and the electronic structure, leading to structural defects such as oxygen vacancies (O_V), and consequently affecting the stability and activity of the catalyst. O_v can be produced by two different cation substitutions, called aliovalent and isovalent substitutions (CHEN et al., 2024). The first process involves the partial replacement of the A matrix cation by an A' cation with a different valence. In this case, O_v are generated to maintain charge neutrality and is often accompanied by the formation of electron-hole and redox pairs. Miao and coworkers (MIAO et al., 2019), for example, have studied the performance of Sr-doped $LaMnO_3$ perovskites in activating PMS. The substitution of La^{3+} by Sr^{2+} ($La_{0.4}Sr_{0.6}MnO_{3-\delta}$) increases the O_v formation due to the lower valence state of Sr ions whereas the electrons in B-sites may leave the covalent bond becoming free electrons and creating holes. Subsequently, adjacent electrons can migrate and fill the electron holes. As a result, the electrical conductivity increases, which improves the persulfate activation in the catalytic performance. In addition, the loss of electrons can result in the variation of the B-site valence state and the formation of a redox pair (Mn^{3+}/ Mn^{4+}), which increased the catalytic activity 6-fold compared to the undoped $LaMnO_3$ perovskite. In addition, the Sr doping introduced magnetic behavior to the mixed oxide, facilitating its recovery and reuse.

Isovalent cationic substitution is the process by which an A' cation of the same valence state partially replaces the A matrix cation. In this case, due to the difference in the two ionic radii, O_v and electron holes are formed, creating strain and distorting the crystal structure (CHEN et al., 2024). A study developed by Ateia et al. (ATEIA; HASSAN; ABDELMAKSOUD, 2021) investigated the partial substitution of La^{3+} by Ce^{3+}, Pr^{3+}, Nd^{3+}, Gd^{3+}, or Sm^{3+} on the structural and magnetic properties of $RE_{0.7}$ La $_{0.3}FeO_3$ perovskites, where RE = Ce, Pr, Nd, Sm and Gd). The results showed that the distortion of the orthorhombic structure increased as the ionic radii of the rare earth elements decreased, resulting from the reduction in the Fe-O-Fe bond angles. Also, it was observed that replacing La^{3+} ions with RE^{3+} changes the spin-orbital coupling and the magnetocrystalline anisotropy. As a result, magnetic properties such as coercivity have changed. In the case of $Sm_{0.7}La_{0.3}FeO_3$, the coercivity was about 19 times higher than that of $LaFeO_3$, as evidenced by the magnetic hysteresis loop.

3.1.4. Influence of the cation present in B-sites on the catalytic properties of perovskites

The choice of B-site cations in perovskite oxides is very important in catalytic processes mainly because of their redox ability. It means that the different valence states of the B-cations influence the electron-transfer capability in oxidation and reduction reactions. In addition to the benefit of redox pairs in multivalent metal sites, the B-element modulation in the lattice can also improve catalytic performance by changing the number and mobility of Ov (WANG et al., 2020).

Studies have shown that introducing metals such as Cu, Mn, Zn, and Co into the B sublattices, without disrupting the crystal structure, leads to the generation of oxygen defects. Furthermore, the transition metal couple can create a synergistic catalytic response. Wang and coworkers (WANG et al., 2019) synthesized Cu-doped $LaFeO_3$ perovskites by the sol-gel method to investigate their catalytic activity toward atrazine degradation. The results demonstrated that introducing Cu into the perovskite structure ($LaCu_{0.2}Fe_{0.8}O_3$ - LCF0.2) significantly enhanced the degradation rate of atrazine. This behavior was attributed to O_v, which facilitated chemical bonding with the oxidizing agent (PMS) and also stabilized lower oxidation states for Fe and Cu. Thus, the mixed valence states (Cu^{2+}/Cu^{1+} and Fe^{3+}/Fe^{2+}) allow for the synergistic relationship between the redox cycles. Similarly, Xie et al. (XIE et al., 2022) introduce Cu into $LaCoO_3$ perovskite catalyst to boost the ciprofloxacin degradation through an electro-Fenton process. The result showed an increase in the degradation rate from 84% ($LaCoO_3$) to 99% ($LaCo_{0.4}Cu_{0.6}O_3$) within 120 min of reaction. In this case, the electron-rich O_v played an important role as both adsorption and reaction sites to capture dissolved oxygen and produce hydroxyl radicals. O_v also promoted charge transfer between Co and Cu species.

3.2. Synthesis methods of perovskites

The synthesis methods used in the preparation of perovskites have an important influence on their crystalline structure, particle and pore size distribution, morphology, and physicochemical properties. Since catalytic reactions typically occur on the catalyst's surface, textural features play a crucial role in determining catalytic efficiency, which is strongly influenced by the synthetic process used to prepare the perovskites (ZHU; ZHANG; DAI, 2015).

There are a variety of techniques to synthesize perovskites and they can be categorized into three main groups: solid phase, liquid phase, and gas phase synthesis.

The solid phase synthesis requires a mixture of precursor powders in the oxide form that should not react to each other at room temperature. This method involves grinding and mixing the starting materials in a ball mill. During the reaction, energy is transferred from the balls to the powders, crushing the reactants, which are then calcinated at high temperatures (900 – 1500 ºC) to form perovskites. The solid-state synthesis is easy to perform but has high energy consumption, and the resulting products tend to have particle sizes in the sub-micrometer range, specific surface areas lower than 2 $m^2.g^{-1}$, lower purity, and uneven size distribution (KUMAR et al., 2020; SOULTATI et al., 2023).

The liquid phase synthesis is widely employed to produce nano-sized perovskites. In this methodology, precursor solutions may react to each other at room temperature (KUMAR et al., 2020). Because of its huge importance in producing perovskites for application in various technological fields, some commonly used liquid-mediated syntheses are described in Table 3.1, highlighting their general procedures, advantages, and usage limitations. The methods used in this work to synthesize all the perovskites will be described in more detail in the 3.2.1 and 3.2.2 sections.

The gas phase synthesis is mainly used to produce thin perovskite films. This method requires special reactors to obtain highly pure perovskites with desired properties. Some examples of gas phase synthesis are thermal evaporation, chemical vapor deposition, and laser ablation (KUMAR et al., 2020; SOULTATI et al., 2023).

Table 3.1 – Examples of liquid phase synthesis methods, their advantages and limitations.

Synthesis Method	General procedures of synthesis	Advantages	Limitations	References
Co-precipitation	-Dissolution of the metal precursors in a suitable solvent, stoichiometric ratios, and temperature (< 100 °C); -Adjustment of the pH by adding a precipitating agent (NaOH, NH_4OH, $C_4H_{13}NO$); -Filtration, washing, and drying the precipitate; -Calcination usually above 550 °C to obtain the crystalline perovskite.	-Straightforward method; -Relatively mild reaction conditions.	-Require control of the pH solution, concentration, stirring speed, and temperature; -Poor uniformity and crystallinity; -Low specific surface area (below 10 $m^2.g^{-1}$).	BACHA et al., 2023; CHEN et al., 2024; KUMAR et al., 2020; MAMBA et al., 2022.
Sol-gel	-Use of the metal precursor solution (nitrate) in stoichiometric ratio; -Addition of the complex agent (CA, ethylene glycol, EDTA); -Formation of "sol" through hydrolysis and partial condensation of complexing agents; -Dehydration of the "sol" and condensation by heat to form "gel" (network structure); -Drying process to collapse the porous network due to the evaporation of the solvent; -Calcination to remove the surface M-OH groups.	-Mild reaction conditions; -Low cost; -Uniform size and morphology; -Possibility of modulating the physical and chemical properties; - Huge surface areas.	-Time-consuming; -May require toxic reactants.	CHEN et al., 2024; MAMBA et al., 2022.
Solvothermal	-Dissolution of the metal precursors in an organic solvent (ethanol, acetone, isopropanol); -Heat treatment in a closed reactor (autoclave) at high pressures and temperatures.	-Ability to yield nanoparticles of uniform morphology and size; -Very efficient to generate a few nanometer-sized oxide; -Production of high-purity	-Require autoclave; -Require high temperatures and pressure; -Require organic solvents; -Time-consuming.	BACHA et al., 2023; CHEN et al., 2024; MAMBA et al., 2022; ROYER et al., 2014.

		crystalline materials.		
Hydrothermal	-Dissolution of the metal precursors in water; -Heat treatment in closed reactors (autoclave) at high pressures and temperatures.	-Eco-friendly; -Ability to yield nanoparticles of uniform morphology and size; -Very efficient to generate a few nanometer-sized oxides; -Production of high-purity crystalline materials.	-Require autoclave; -Require high temperatures and pressure; -Time-consuming.	BACHA et al., 2023; CHEN et al., 2024; MAMBA et al., 2022; ROYER et al., 2014.

3.2.1. Conventional citrate method

Among the synthesis methods used to obtain perovskite oxides, the conventional citrate method has been considered an efficient route. It uses soluble metal nitrates as precursors and citric acid (CA) as an organic complexing agent to coordinate the metal ions. The formation of citrate complexes enables the well-dispersion of the metal cations in the matrix. After calcination, typically performed at temperatures in the range of 700 ºC to 900 ºC for 2-6 h, metal oxide nanoparticles are obtained. Materials prepared by this method typically exhibit a relatively low specific surface area, generally less than 10 $m^2.g^{-1}$. Nevertheless, its widespread use can be attributed to the method's ease of operation, simple design, and capacity to achieve high homogeneity and precursor dispersion. These features allow the composition and catalytic activity of the prepared materials to be fine-tuned (LEONEL et al., 2024; ZHU; ZHANG; DAI, 2015; ZHU et al., 2014).

Some strategies have been developed to obtain perovskites with improved surface area, including the use of silica templates. In this case, porosity is created in the perovskite catalysts, overcoming the small specific surface area drawback.

3.2.2. Nanocasting method

Since its first discovery, ordered mesoporous materials have attracted much interest due to their high surface area, large pore volume, and controlled pore structure. Particularly, ordered mesoporous metal oxides have received much attention due to their highly porous structure, which favors optical, electronic, biological, and catalytic applications (ROYER et al., 2014; WANG et al., 2008).

Mesoporous perovskites have usually been synthesized using nanocasting with silica (SBA-15, SBA-16, KIT-6) as a hard template. The experimental procedures selected to produce perovskites by this approach are illustrated in Fig. 3.2. First, silica with regular porosity is produced, and then metal precursor solution is infiltrated inside nanospaces confined by the pore channels of the silica template. The usage of confined spaces is of huge importance due to the restriction of particle growth during the synthesis, which facilitates the development of nanostructures. After suitable infiltration, the composite is heat treated at high temperature (700 ºC to 900 ºC) for the perovskite crystallization. The silica host is then selectively

removed by washing with an alkaline solution (e.g., NaOH), opening up new pores in the resulting perovskite. The ideal condition is the presence of interconnected pore channels in the hard template, allowing the formation of perovskites with an inverse replica of the template. Materials acquired in this way exhibit organized porosity in the mesodomain range and remarkable textural properties that highly improve catalytic activity (ROYER et al., 2014; THOMAS et al., 2024; ZHU; ZHANG; DAI, 2015). Recent work (AFZAL et al., 2025) has investigated the influence of surface area on the catalytic activity of $LaCoO_3$. They synthesized nanocast NC-$LaCoO_3$ as a PMS catalyst using the mesoporous silica KIT-6 (tridimensional material, first fabricated at Korea Advanced Institute of Science and Technology) as a hard template. The catalytic efficiency of NC- $LaCoO_3$ was compared with the $LaCoO_3$ synthesized by the citric acid-assisted method (CA- $LaCoO_3$). The NC-$LaCoO_3$ showed a higher specific surface area (81 $m^2.g^{-1}$) than CA-$LaCoO_3$ (3 $m^2.g^{-1}$) and also much higher catalytic activity (100% of atrazine degradation within 4 min *vs.* 58% in 6 min) considering the same reaction conditions for the experiments.

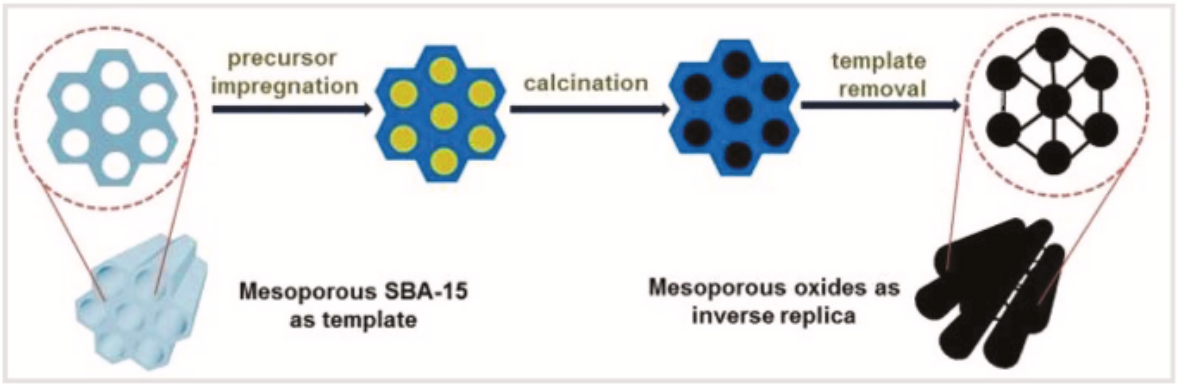

Figure 3.2 – Schematic representation for the nanocasting synthesis using the ordered mesoporous SBA-15 as a hard template (ROYER et al., 2014).

Silica is one of the existing templates for the development of mesoporous metal oxides. Other possibilities include porous carbon, zeolites, and polymers. However, mesoporous SiO_2 offers several advantages for producing highly ordered porous structures with tailored chemical and textural properties. They exhibit high thermal stability, which allows the calcination process to occur at higher temperatures. Their flexibility for chemical modifications through the attachment of organic groups can enhance their selectivity due to the creation of interactions, such as electrostatic forces, hydrophilic or hydrophobic interactions, covalent bonds, and

hydrogen bonding. In addition, the pore dimension, morphology, and structure of mesoporous silica can be easily altered (LU; ASTRUC, 2020; THOMAS et al., 2024).

Usually, mesoporous silica can be divided into a varied of series, including SBA (Santa Barbara Amorphous), KIT (Korean Advanced Institute of Science and Technology), HMS (Hollow Mesoporous Silica), and MCM (Mobile Composition Matter), as displayed in Fig. 3.3. Each one is distinguished by the type and shape of mesoporous, which influence on the wetting properties of the base material (THOMAS et al., 2024).

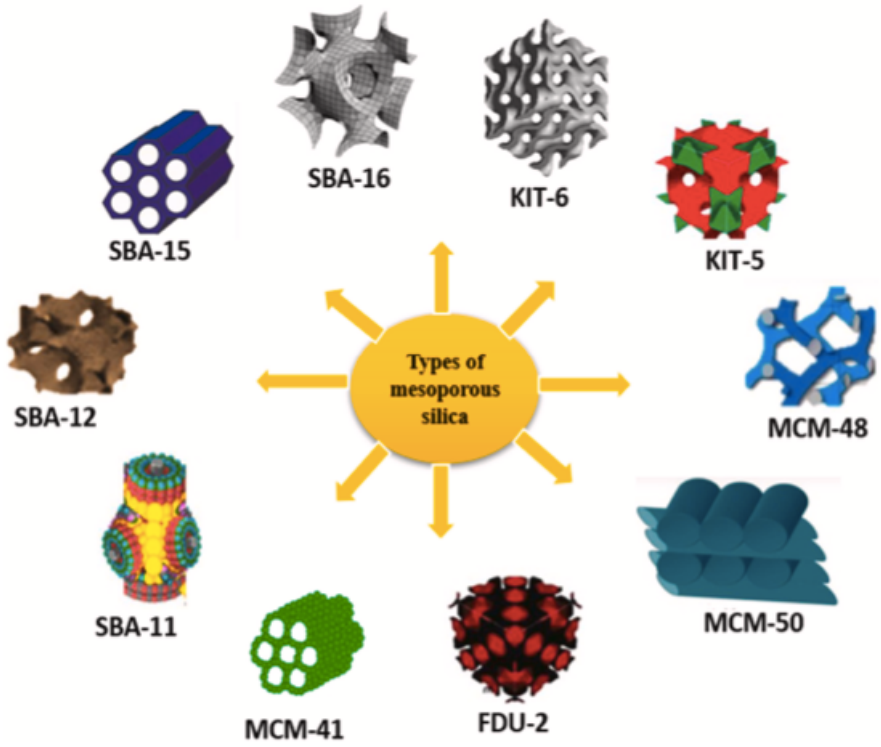

Figure 3.3 – Types of mesoporous silica based on their shapes (THOMAS et al., 2024).

3.3. Applications of La-based perovskites in adsorption and catalysis for water remediation

3.3.1. Organic water contaminants

The increasing discharge of diverse organic contaminants into water systems has significantly impacted water quality, resulting in adverse effects on human health and the ecosystem. Although most of the reported studies have explored the removal of organic dyes, such as methylene blue, crystal violet, congo red, and methyl orange, there are other alarming contaminants, including pharmaceutical and personal care residues, pesticides, and industrial compounds or by-products that even at low concentration (ng/L or μg/L) can be conceivably toxic (RODRIGUEZ-NARVAEZ et al., 2017).

The effective treatment of pharmaceutical residues is of great interest due to their chemical stability, which makes them difficult to biodegrade and consequently inappropriate for disposal. Most of these active compounds come into the domestic water through excretion and, subsequently, can enter into the environment due to the inefficient wastewater treatment plants. Some examples of pharmaceutical products comprise antibiotics (*e.g.,* amoxicillin and tetracycline), anticancer drugs (*e.g.,* doxorubicin), anti-inflammatory (*e.g.,* ibuprofen and diclofenac), anticonvulsant (*e.g.,* carbamazepine), and hormones (*e.g.,* progesterone) (LU; ASTRUC, 2020; ROJAS; HORCAJADA, 2020).

Among numerous organic industrial chemicals, phenolic and related aromatics are widely used in manufacturing processes. Particularly, nitrophenols and their derivatives have gained worldwide attention as water pollutants because they are broadly used to produce dyes, pharmaceuticals, pesticides, and explosives, although their high potential toxicity to humans and aquatic organisms, carcinogenicity, and bioaccumulation (XIONG et al., 2019). Figure 3.4 presents the molecular structures of different water contaminants. The functional groups present in these products, including $-OH$, $-COOH$, $-NH_2$, $-CONH_2$, $-SO_2$ have interaction affinity that can facilitate surface adsorption through electrostatic and covalent attachment (LU; ASTRUC, 2020).

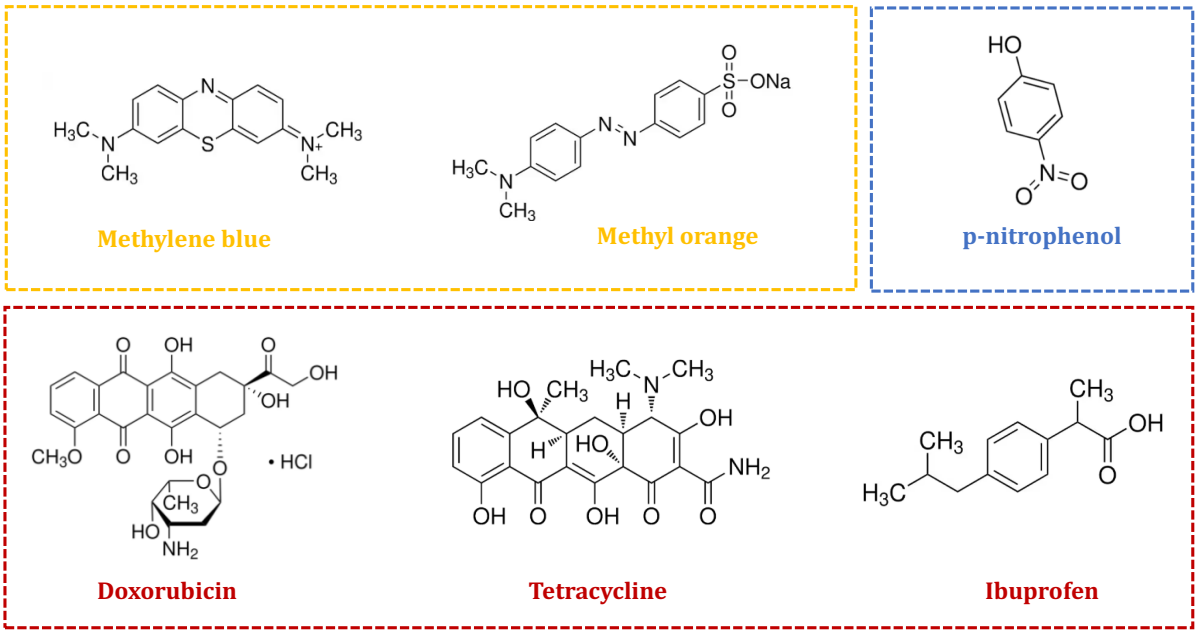

Figure 3.4 – Molecular structures of different water contaminants. Adapted from (LU; ASTRUC, 2020).

3.3.2. Adsorption

Due to its low cost, simple design, and ease of operation, adsorption is widely used in various water treatment technologies. This technique is versatile and effective in targeting a broad range of contaminants. However, the effectiveness of the process depends on the surface physicochemical properties of the adsorbent. Therefore, when evaluating adsorptive materials, it is essential to consider key features such as specific surface area, active sites, and other surface characteristics (IBRAHIM et al., 2024).

The specific surface area of the material is one of the physical indicatives of adsorption performance and is directly correlated with the adsorption sites. This means that, for a given pore volume, more adsorption sites can be exposed to the contaminant as the SSA increases. On the other hand, SSA is inversely correlated with the pore size. Macroporous structures, for example, reduce the mass transfer resistance, which is convenient for the fast diffusion of pollutants in the adsorbent and also the fast association with the active sites to improve the adsorption kinetics (HUANG et al., 2023).

The chemical bonding between the adsorption site and the contaminant also plays an important role in this process. The B-site of a perovskite, being a transition metal and

connected to oxygen atoms, can coordinate with specific groups in pollutants due to electron transfer (HUANG et al., 2023).

Besides surface characteristics, other factors affect the rate of adsorption in a solution, such as temperature, pH, and concentration of both the adsorbent and contaminant. The pH of the medium influences the electrostatic charge on the surface of the adsorbent, which in turn affects their binding affinity to ionized contaminant molecules. To better understand this phenomenon, it is important to know the point of zero charge (PZC) of the adsorbent, defined as the pH at which the surface is electrically neutral. Although increasing the amount of adsorbent usually increases the adsorption efficiency, excessive quantities may lead to agglomeration and a decrease in the adsorption capacity (IBRAHIM et al., 2024).

3.3.3. Advanced Oxidation Processes

3.3.3.1. Fenton and Fenton-like processes

Traditionally, the Fenton process involves the decomposition of H_2O_2 to generate OH radicals ($HO^{\bullet}$) through catalytic reaction with ferrous ions (Fe^{2+}), according to Equation 3.4. The $HO^{\bullet}$ can attack organic contaminants generating an organic radical ($R^{\bullet}$), which undergoes a sequence of chemical transformation, generating different oxidation products (BABUPONNUSAMI; MUTHUKUMAR, 2014). The Fe^{2+} species can be regenerated in an efficacious cyclic mechanism through Fenton-like reactions, which consist of the reduction of the resulting ferric ions by the excess of H_2O_2 (Equation 3.5). There also occurs a formation of hydroperoxyl radicals ($HO_2^{\bullet}$) that can oxidize organic pollutants, but with less sensitivity than $HO^{\bullet}$ because they have weaker oxidation capacity ($E^0 = 1.65$ V) (BABUPONNUSAMI; MUTHUKUMAR, 2014; MIRZAEI et al., 2017).

$$Fe^{2+}_{(aq)} + H_2O_{2(aq)} \rightarrow Fe^{3+}_{(aq)} + OH^{\bullet} + OH^-_{(aq)} \quad (3.4)$$

$$Fe^{3+}_{(aq)} + H_2O_{2(aq)} \rightarrow Fe^{2+}_{(aq)} + HO_2^{\bullet} + H^+_{(aq)} \quad (3.5)$$

Relying on the reactive phase, these reactions can be classified as homogeneous or heterogeneous. The essential difference is that the catalytic process takes place in the liquid phase in the homogeneous system, while it occurs on the catalyst surface in the heterogeneous

system (WANG et al., 2016), as depicted in Figure 3.5.

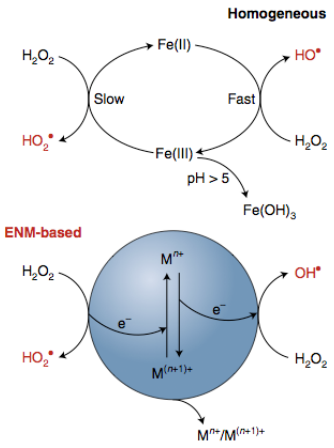

Figure 3.5 – Schematic representation of the redox cycle in the homogeneous Fenton reaction and the surface of engineered nanomaterial (ENM) catalyst (HODGES; CATES; KIM, 2018).

Fenton and related processes have been extensively investigated for removing various pollutants in water treatment, such as pharmaceuticals, textiles, and chemical pesticides. Considering that these reactions are affected by some parameters including pH, the concentration of H_2O_2 and catalyst, temperature, and pollutant concentration, the systematic study of these variables is of utmost importance to enhance the catalytic properties of the system (BELLO; RAMAN; ASGHAR, 2019).

The pH of the medium is one of the most critical parameters for effective wastewater treatment. Some studies have reported that $HO^{\bullet}$ production is efficient when the pH is in the range of 2.8-3.5. (HODGES; CATES; KIM, 2018) (ARIMI et al., 2020; HODGES; CATES; KIM, 2018) Under acidic conditions, Fe(II) and Fe(III) species can preserve their catalytic capability, while higher pH causes the precipitation of ferric ions as iron hydroxide (BELLO; RAMAN; ASGHAR, 2019). On the other hand, studies showed that it is possible to acquire nanosystems with suitable activity in neutral and even in alkaline pH conditions.

Another pivotal parameter that plays an important role in the catalytic activity is Fenton's reactants. The concentration of hydrogen peroxide dictates the potential for $HO^{\bullet}$ generation. Insufficient H_2O_2 concentration can lead to a deficiency of radicals generation, which might

result in a decrease in pollutant oxidation (WANG et al., 2016). On the other hand, an excess concentration of H_2O_2 can induce a scavenge effect according to Equation 3.6, contributing to the decrease in the treatment efficiency as well (BELLO; RAMAN; ASGHAR, 2019). Hence, large quantities of oxidants are not recommended.

$$H_2O_{2(aq)} + HO^{\bullet} \rightarrow H_2O_{(l)} + HO_2^{\bullet} \quad (3.6)$$

In the same way, Fe(II) catalyst concentration should be optimized to ensure ideal hydroxyl radical production and avoid the scavenging effect, supposing an excess amount of ferrous ions (Equation 3.7) (ARIMI et al., 2020; BABUPONNUSAMI; MUTHUKUMAR, 2014; BELLO; RAMAN; ASGHAR, 2019).

$$Fe^{2+}_{(aq)} + HO^{\bullet} \rightarrow Fe^{3+}_{(aq)} + OH^-_{(aq)} \quad (3.7)$$

The effect of temperature on the contaminant degradation rate is a controversial issue. Some studies have demonstrated that high temperatures adversely affect the Fenton reactions due to the potential decomposition of H_2O_2 into H_2O and O_2. Conversely, recent studies have shown that high temperatures (in the range of 40 °C to 90°C) favor the oxidation rate, which enhances the generation of $HO^{\bullet}$ and improves, therefore, the Fenton reactions. However, ambient conditions can securely be used with good efficiency in this process (BABUPONNUSAMI; MUTHUKUMAR, 2014; BELLO; RAMAN; ASGHAR, 2019).

The effect of increasing the concentration of the contaminant has been proven to decrease the removal efficiency in the case of maintaining constant other parameters, such as the concentration of the catalyst. It occurs mainly because of two reasons - higher pollutant concentrations demand higher concentrations of radicals and a higher number of active sites, which can become limited when the dosage of pollutants is too high. To this end, these circumstances indicate that the initial contaminant concentration is responsible for determining the optimum Fenton's reactant concentration to ensure great reactivity and effective water treatment (MIRZAEI et al., 2017).

3.3.3.2. Sulfate radical based-processes

Another promising AOP for removing water contaminants is based on sulfate radicals. They exhibit many advantages over $^{\bullet}OH$-based processes, such as Fenton and Fenton-like processes. Firstly, the most important oxidants (i.e., persulfates-PS; $S_2O_8^{2-}$ and peroxymonosulfate-PMS; HSO_5^-) frequently used to generate sulfate radicals ($SO4^{\bullet-}$) are considered cheaper and more stable than both H_2O_2 and O_3 for water purification (HODGES; CATES; KIM, 2018). Secondly, sulfate radicals display comparable oxidation potential to $HO^{\bullet}$ (E^0 = 2.5- 3.1 V *vs.* 2.8 V) and longer half-life time (30-40 μs vs. 20 ns). Finally, they can operate in aqueous systems on a wide pH range (from 2 to 8) and are usually considered an environmentally benign process (XIAO et al., 2020). Although different transition metals (Co, Mn, Cu, Fe, Ni, Zn) can be used to activate PS or PMS either in homogeneous or heterogeneous systems, iron is the most used activator mainly due to its high effectiveness and lower potential toxicity (XIAO et al., 2020). The activation of PS and PMS with iron species in a homogeneous way has been commonly performed owing to its low-cost and straightforward operation. However, some drawbacks have motivated the use of heterogeneous catalyzes, such as the requirement of separation and further disposal of iron sludge and a greatly pH-dependent system to avoid precipitation of iron species. The activation mechanism of PS by ferrous ions is described by Eq. 3.8. As for Fe(II) activating PMS, two pathways are feasible, giving rise to hydroxyl or sulfate radicals, according to Eqs. 3.9 and 3.10. It can also react with the ferric species, inducing the formation of the sulfur pentoxide radical ($SO_5^{\bullet-}$), which is less reactive compared to the sulfate radical but can degrade contaminants, as illustrated in Eq. 3.11.

$$Fe^{2+} + S_2O_8^{2-} \rightarrow Fe^{3+} + SO_4^{\cdot-} + SO_4^{2-} \quad (3.8)$$

$$Fe^{2+} + HSO_5^- \rightarrow Fe^{3+} + SO_4^{\cdot-} + OH^- \quad (3.9)$$

$$Fe^{2+} + HSO_5^- \rightarrow Fe^{3+} + SO_4^{2-} + OH^{\cdot} \quad (3.10)$$

$$Fe^{3+} + HSO_5^- \rightarrow Fe^{2+} + SO_5^{\cdot-} + H^+ \quad (3.11)$$

4. MATERIALS AND METHODS

A schematic representation of the experimental design developed in this study is presented in the Figure 4.1.

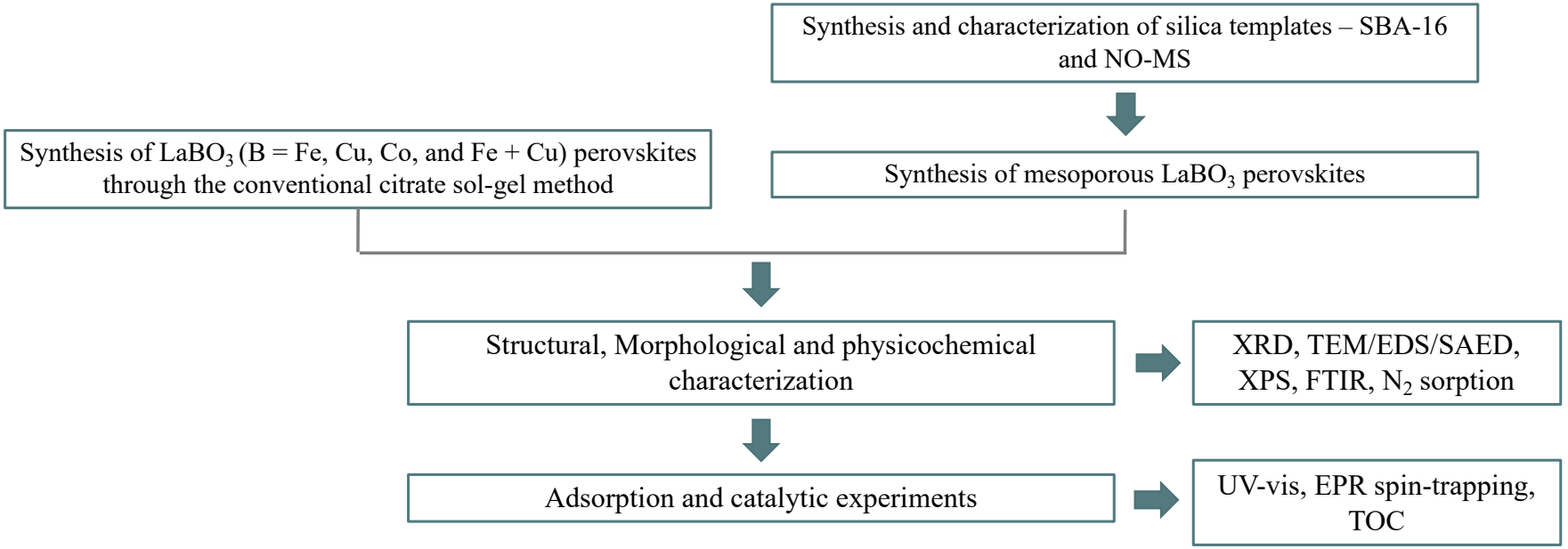

Figure 4.1 – Experimental procedures.

4.1. Synthesis of La-based perovskites ($LaBO_3$)

4.1.1. Materials

Lanthanum (III) nitrate hexahydrate ($La(NO_3)_3.6H_2O$, 99.9%, Aldrich), iron (III) nitrate nonahydrate ($Fe(NO_3)_3 \cdot 9H_2O$, 98%, Synth), copper (II) nitrate hexahydrate ($Cu(NO_3)_2 \cdot 6H_2O$, 99.9%, Aldrich), cobalt (II) nitrate hexahydrate ($Co(NO_3)_2 \cdot 6H_2O$, 98%, Êxodo Científica) citric acid (CA, 99%, Sigma-Aldrich), and deionized water (DI water, Millipore Simplicity™) with a resistivity of 18 MΩ.cm at 25 ºC without further purification.

4.1.2. Methods

La-based perovskites were prepared by a similar method previously reported (ALCAMAND et al., 2022), as illustrated in Figure 4.2. $La(NO_3)_3$ and $Fe(NO_3)_3$ were used as precursors, while CA was used as a complexing agent. Briefly, CA and nitrates were dissolved in 30 mL of DI water at room temperature (RT) in the following sequence: CA, $Fe(NO_3)_3$, and $La(NO_3)_3$. The molar ratio of Ca/(La+Fe) was kept at 1:1. The as-prepared solution was homogenized under moderate stirring for 3 h at room temperature to create a citrate complex of metal cations. Subsequently, the solution was heated to 80 °C until the complete evaporation of water, giving rise to a solid material. This powder was then air-calcined at 550 °C for 2 h and at 750 °C for 6 h using a heating rate of 1 °C min^{-1} to eliminate CA/nitrate ions and to bring about the $LaFeO_3$ (LFO) perovskite crystal lattice, respectively. The synthesis of La_2CuO_4 (LCuO) and $LaCoO_3$ (LCoO) was similar to LFO except for the precursor used. In these cases, $Fe(NO_3)_3$ was replaced by $Cu(NO_3)_2$ and $Co(NO_3)_2$, respectively. The effect of B-sites composition was also investigated by replacing 10% mol of Fe^{3+} species with Cu^{2+} species, resulting in a Cu-doped $LaFeO_3$ perovskite ($LaCu_{0.1}Fe_{0.9}O_3$ – LCuFO).

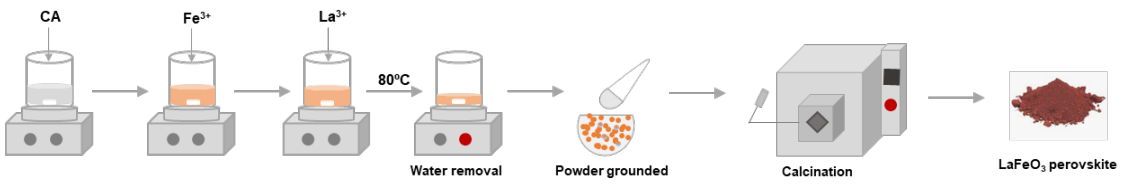

Figure 4.2 – Schematic representation of the synthesis of La-based perovskites.

4.2. Synthesis of mesoporous La-based perovskites

4.2.1. Materials

Hydrochloric acid (HCl, 37% v/v, Aldrich), poly (ethylene oxide)-poly (propylene oxide)-poly (ethylene oxide) triblock copolymer (Pluoronic® F-127, Sigma-Aldrich), tetraethyl orthosilicate (TEOS, 98%, Sigma-Aldrich), sodium hydroxide (NaOH, 98%, Aldrich), ethanol (EtOH, 99.8%, Aldrich), lanthanum (III) nitrate hexahydrate ($La(NO_3)_3.6H_2O$, 99.9%, Aldrich), iron (III) nitrate nonahydrate ($Fe(NO_3)_3 \cdot 9H_2O$, 98%, Synth), copper (II) nitrate hexahydrate ($Cu(NO_3)_2 \cdot 6H_2O$, 99.9%, Aldrich), cobalt (II) nitrate hexahydrate ($Co(NO_3)_2 \cdot 6H_2O$, 98%, Êxodo Científica), citric acid (CA, 99%, Aldrich), and deionized water (DI water, Millipore Simplicity™) with a resistivity of 18 MΩ.cm at 25 ºC without further purification.

4.2.2. Methods

4.2.2.1. Synthesis of the ordered porous silica (SBA-16) template

SBA-16 was prepared following a similar procedure described by (GOMES et al., 2021). In a typical synthesis, F-127 was initially dissolved at room temperature under stirring for 2 h in a DI water and HCl solution. Next, TEOS was dropwise added to this acidic solution under continuous stirring at RT (TEOS: H_2O: HCl: F127 molar ratio = 1: 147: 4: 0.008). The obtained solution was kept under stirring for 24 h to favor the complete hydrolysis of the silicon precursor before condensation took place. The solution was aged at 80 ºC in a closed flask for 24 h. The obtained solid was washed with H_2O and then air-dried overnight at 80 ºC. Subsequently, it was air-calcined at 500 ºC at a heating rate of 1 ºC min^{-1} for 6 h to promote the thermal degradation of Pluronic® F-127 from silica. The removal of this template is mandatory to give rise to an open and ordered mesoporous silica.

4.2.2.2. Synthesis of the non-ordered mesoporous silica (NO-MS)

NO-MS template was prepared following a similar procedure (MOTA et al., 2019). Initially, a mixture of EtOH and DI H_2O was prepared at room temperature. TEOS, the silicate precursor, was then slowly added under vigorous stirring. The TEOS: H_2O: EtOH molar ratio

was adjusted to 1: 20: 4. These solutions were stirred at room temperature for 30 min, aged in a closed bottle for 24 h at 90 °C for complete gelation of the solution, and the obtained solids were then dried at 90 °C. Subsequently, gels were washed with DI H_2O to eliminate the residual ethoxy groups from the TEOS precursor and dried at 90 °C overnight. Finally, the template was powdered with an agate mortar.

4.2.2.3. Synthesis of mesoporous La-based perovskites

The synthesis of nanocast mesoporous perovskites was conducted by the wet precursor impregnation on silica (SBA-16 or NO-MS), using a solution of CA and EtOH as a complexing agent. Initially, a mixture of EtOH and DI water was prepared (3:1 v/v, EtOH: H_2O) (ALCAMAND et al., 2022). Next, CA was added under stirring, and the molar ratio between total metal cations and CA was kept at 1:1. Subsequently, the nitrate precursor species were added to this alcoholic solution that was stirred for 2 h until its complete homogenization. In another flask, SBA-16 or NO-MS was dispersed in DI H_2O and kept under stirring for 2 h at room temperature. Next, the solution containing the metal ion precursors was dropwise added to the beaker containing the silica dispersion. This mixture was stirred for 3 h at room temperature. Subsequently, the system was heated up to 80 ºC to promote the evaporation of solvents (EtOH and H_2O) and air-dried at the same temperature for 24 h, giving rise to a solid material that was powdered with an agate mortar. Thus, after the impregnation of the silica template by the precursor solutions, a heat treatment was applied to obtain the perovskite-type oxides as follows. Firstly, a heating rate of 1 ºC min^{-1} was used to increase the temperature of the powder from RT up to 550 ºC, and the material was kept at this temperature for 2 h. Secondly, the material was heated up to 750 ºC at a rate of 1 ºC min^{-1} and maintained at this temperature for 6 h. Finally, it was cooled down to the RT. The obtained material was pulverized, and then the silica mold was removed by washing the composite three times with a NaOH solution (2 $mol.L^{-1}$) at room temperature. Finally, the product was rinsed with H_2O until the solution pH reached 7 and air-dried for 24 h at 80 °C. Figure 4.3 displays a schematic representation of the procedure for preparing perovskites from the nanocasting approach (LCuFO_SBA-16 and LCuFO_NO-MS).

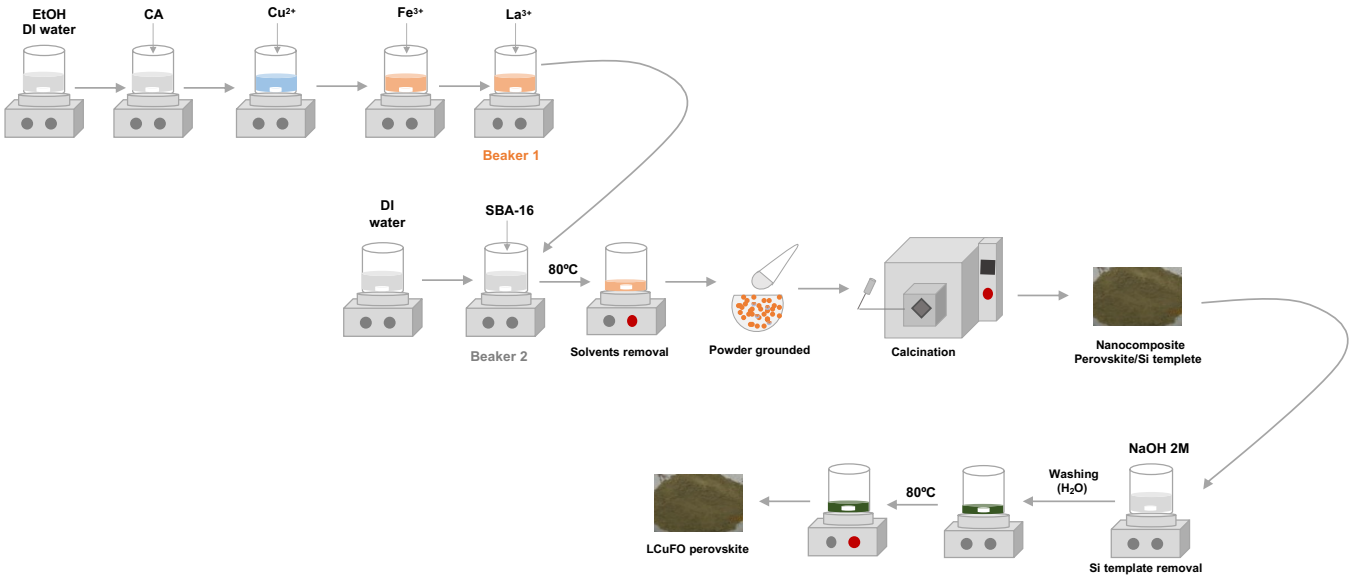

Figure 4.3 – Schematic representation of the synthesis of La-based perovskites/SBA-16 or NO-MS from the nanocasting method.

4.3. Structural, morphological, and physicochemical characterization of La-based perovskites

4.3.1. X-ray Diffraction (XRD)

X-ray diffraction (XRD) was performed on a PANalytical Empyrean diffractometer (Almelo, Netherlands) using Cu-Kα radiation (λ = 1.54 Å). The XRD patterns were recorded in the 2θ range from 3 to 90˚ at a scanning speed of 0.06˚s^{-1}. The small-angle X-ray patterns of the Si templates were recorded in the 2θ range from 0.4 to 4˚ at a scanning speed of 0.02˚s^{-1}. The diffractograms were analyzed using the X'Pert High Score software and compared with the International Center for Diffraction Data (ICDD) database. The crystallite size of the materials was estimated using the Scherrer equation (FATIMAH et al., 2022).

4.3.2. Transmission Electron Microscopy (TEM)

TEM images, selected-area electron diffraction (SAED) patterns, and energy-dispersive X-ray (EDS) spectra were performed on an FEI Tecnai G2- F20 microscope (Inc., Hillsboro, USA) at an accelerating voltage of 200 kV. The samples used in these studies were first dispersed in absolute ethanol under sonication for about 5 min at RT. They were then dripped onto carbon-

coated copper or nickel grids (in the case of perovskites containing Cu in their composition) and air-dried at RT.

4.3.3. X-ray Photoelectron Spectroscopy (XPS)

XPS analysis was performed using a Specs Phoibs 150 spectrometer equipped with a monochromatic Al-Kα X-ray excitation source. For accuracy, all peak positions were corrected using the C 1s binding energy (284.6 eV) as the reference.

4.3.4. Fourier Transformed Infrared Spectroscopy (FTIR)

FTIR analysis was performed using a Bruker Alpha spectrometer with a resolution of 4 cm^{-1} and 128 scans. An Attenuated Total Reflectance (ATR) accessory equipped with a diamond crystal was used in these tests.

4.3.5. N_2 sorption

N_2 sorption tests were carried out on Micromeritics ASAP 2020 and Quantachrome Autosorb IQ2 systems. The samples were previously outgassed under vacuum at 300 °C for 3 h to remove humidity and impurities. The specific surface area (SSA) was inferred using the Brunauer-Emmett-Teller (BET) model.

4.4. Catalytic degradation activity study

The catalytic degradation performance of the perovskites was evaluated by measuring the degradation rate of MB using both Fenton-like and sulfate radical-based reactions. Experiments were performed at room temperature using aqueous dispersions of LFO, LCuO, LCoO, LCuFO, and mesoporous LCuFO. Before adding oxidants (H_2O_2 or PMS), the materials were stirred in the dark for 1 h to achieve adsorption-desorption equilibrium. At predetermined intervals (0, 5, 20, 40, 60, 90, and 120 min), 4 mL aliquots of the suspensions were collected and centrifuged at 4000 rpm for 10 min. The particle-free supernatant was then transferred to plastic cuvettes and examined by UV–vis spectroscopy. The Beer-Lambert law was used to establish a correlation between the measured absorbance and concentration at 664

nm, the wavelength of maximum absorption of MB. The photodegradation kinetics of the contaminant were studied using the Langmuir-Hinshelwood model and varying the concentration of MB. The catalytic performance of the perovskites was investigated by varying several parameters, including solution pH, catalyst to MB dosing rate, oxidant type (H_2O_2 or PMS), and its concentration. EPR coupled with the spin-trapping technique was used to investigate the mechanisms of MB degradation. This method identifies short-lived free radicals, especially reactive oxygen species (ROS) (GONÇALVES et al., 2019). EPR studies were performed with a 9.4 GHz Magnettech MiniScope MS400 X-band spectrometer. Spin-trapping was performed with 5,5-dimethyl-1-pyrroline N-oxide (DMPO, Oakwood, 96%) as a trapping agent. The mineralization rate of MB was evaluated using a Shimadzu Total Organic Carbon (TOC) analyzer following the guidelines outlined in the Standard Methods for Examination of Water and Wastewater (ALPHA; AWWA; WEF, 2012).

Figure 4.4 schematically represents the steps followed to evaluate the catalytic performance of the perovskites, considering the studied parameters. Table 4.1 exhibits the reasons for the chosen values.

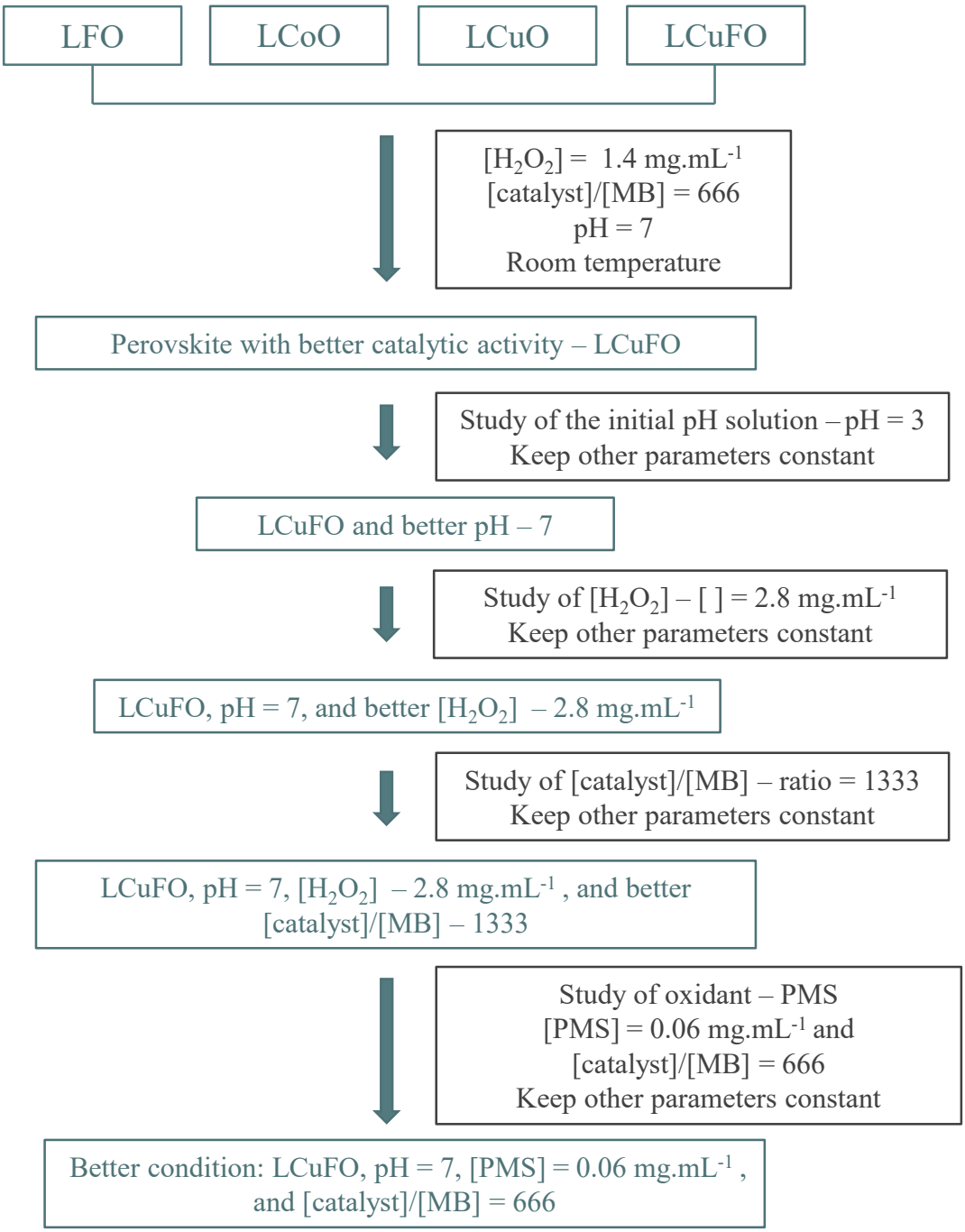

Figure 4.4 – Schematic representation of the experimental matrix developed to evaluate the catalytic activity of perovskites.

Table 4.1 – Summary of the parameters used in the experiments and the reason for the chosen values.

Parameters of Study	Values	Reasons
Transition metal at B-site	Fe Cu Co	These species provide different redox cycles towards the oxidants, which may generate different amounts of free radicals, and consequently dissimilar catalytic activities (BOKARE; CHOI, 2014a).
Initial pH solution	3 7	Fe/H_2O_2 Fenton systems work better in acidic conditions, whereas Cu/H_2O_2 Fenton-like systems have the potential to work well over a broader pH range, mostly at near-neutral conditions (BOKARE; CHOI, 2014a)
[Catalyst]/[MB] ratio	666 (HP)[a] 1333 (HP)[b] 666 (PMS)[c]	Increasing the concentration of catalyst, keeping constant the concentration of pollutant, i.e., increasing the catalyst/pollutant loading ratio can increase the number of active sites, therefore increasing the catalytic efficiency (BELLO; RAMAN; ASGHAR, 2019)
[Oxidant]	1.4 mg/mL (HP) 2.8 mg/mL (HP) 0.06 mg/mL (PMS)	High oxidant concentration favors the generation of free radicals (ARIMI et al., 2020; BELLO; RAMAN; ASGHAR, 2019)

a = [catalysts] = 2 mg/mL and [MB] = 3 μg/mL
b = [catalysts] = 4 mg/mL and [MB] = 3 μg/mL
c = [catalysts] = 2 mg/mL and [MB] = 3 μg/mL

5. RESULTS AND DISCUSSION

5.1. $LaBO_3$ perovskites

5.1.1. Structural and physicochemical characterization of $LaBO_3$

Powder X-ray diffraction (XRD) is a powerful technique for identifying crystalline phases and crystallite size in a sample. The XRD pattern of LFO is shown in Fig. 5.1a(i), revealing the formation of orthorhombic $LaFeO_3$ (JCPDS card No. 37-1493). The diffraction peaks observed at 2θ values of 22.6°, 32.2°, 39.7°, 46.1°, 52.5°, 53.3°, 57.4°, 67.3°, and 76.6° correspond to the crystal planes (101), (121), (220), (202), (141), (311), (240), (242), and (313), respectively. Notably, there is no evidence for the formation of additional Fe or La oxides. The XRD pattern of LCuFO, exhibited in Fig. 5.1a(ii), has similar diffraction peaks to those observed for LFO, suggesting that the substitution of 10 mol % Fe^{3+} by Cu^{2+} species has not influenced the orthorhombic structure of the Fe-La oxide (PHAN et al., 2018). On the other hand, the XRD pattern of LCuO, displayed in Fig. 5.1b, reveals the presence of crystal phases characterized by the structural formula A_2BO_4. These oxides consist of alternating ABO_3 and AO layers and are commonly referred to as "perovskite-like oxides" (ZHU et al., 2014). In addition to orthorhombic La_2CuO_4 (JCPDS card No. 30-0487), monoclinic CuO (JCPDS card No. 05-0661) has also been observed in this material. The preferential formation of La_2CuO_4 over $LaCuO_3$ may be related to the stability of Cu^{x+} species. At atmospheric pressure, the La_2CuO_4 oxide, which contains Cu^{2+} cations, is the only mixed oxide in the La_2O_3-CuO phase diagram. As reported in the literature, the stabilization of highly oxidized Cu^{3+} species, as observed in $LaCuO_3$, requires oxygen pressures up to 6.5 GPa (DIAS et al., 2020; FALCÓN et al., 2000). Since the synthesis method in this study for Cu-La oxide follows the conventional citrate approach at 750 °C and 1 atm, the predominant crystal phase is La_2CuO_4. Fig. 5.1c depicts the XRD pattern of LCoO, revealing the presence of a single-phase structure, specifically the rhombohedral Co-La oxide (JCPDS card No. 48-0123). The 2θ peaks identified at 23.2°, 32.8°, 33.9°, 40.6°, 41.3°, 47.5°, 53.2°, 53.8°, 58.9°, 59.7°, 68.9°, 69.9°, 73.8°, 74.3°, 78.7°, 79.4°, and 83.6° correspond to the crystal planes (012), (110), (104), (202), (006), (024), (122), (116), (214), (180), (220), (208), (312), (306), (134), (128), and (226), respectively. The crystal size (τ) of the prepared oxides was evaluated from the obtained XRD patterns using the Scherrer equation. The results presented in Fig. 5.1d show

that τ values for La-based perovskites are in the range of 20-22 nm. However, τ values for the LCuO sample are not shown due to the presence of a secondary phase (CuO) detected in its structure in addition to La_2CuO_4, through the Rietveld refinement. This sample was found to contain approximately 18 wt% CuO and 82 wt% La_2CuO_4. The coexistence of these two phases could introduce errors in the calculation of τ. Notably, changing the B-site transition metal did not significantly affect the crystal size. This observation can be attributed to the minor differences in ionic radii among the Fe, Co, and Cu species incorporated into the perovskite B-site, underscoring the flexibility of these mixed metal oxides.

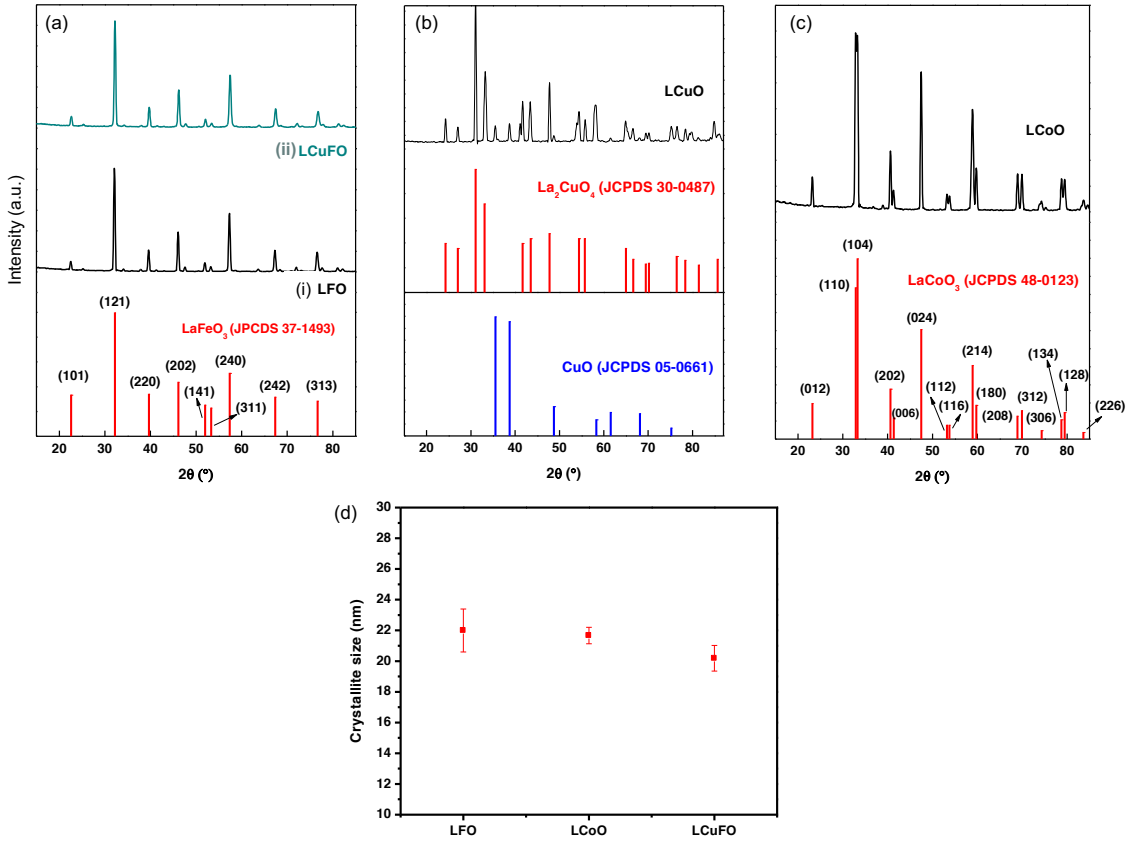

Figure 5.1 – XRD patterns of (a-i) LFO, (a-ii) LCuFO, (b) LCuO, and (c) LCoO perovskites. (d) crystallite size evaluated by the Scherrer equation (n = 4; mean ± standard deviation; one-way ANOVA followed by Bonferroni's test with $p < 0.05$). The calculated crystallite sizes were not found to be significantly different.

Figs. 5.2-5.4a show TEM micrographs obtained for the prepared perovskites. As reported in the literature, agglomerated particles with irregular morphology were observed in all samples (ALCAMAND et al., 2022; ATEIA; HASSAN; ABDELMAKSOUD, 2021; ZHANG et al., 2023). These properties are expected for citrate-derived perovskites due to the required heat

treatment conditions, including high temperatures (550-750 °C) and extended calcination times (2-6 h). Nevertheless, these conditions allow the formation of high-purity materials (ALCAMAND et al., 2023; KUCHARCZYK et al., 2020).

EDS analyses were performed to evaluate the composition of the LCuFO perovskite. As expected, the presence of La, Cu, Fe, and O is confirmed by the EDS spectrum of Fig. 5.2b.

High-resolution TEM images, as shown in Fig. 5.2c and Figs. 5.3-5.4c, reveals interference fringes, confirming the polycrystalline nature of the materials. The SAED pattern in Fig. 5.2d shows concentric ring patterns characteristic of Bragg diffraction. These patterns were associated with crystal planes {121} and {101}, which are consistent with the characteristic lanthanum ferrite perovskites (PHAN et al., 2018; RAO et al., 2018), as discussed earlier in the XRD analysis (Fig. 5.1).

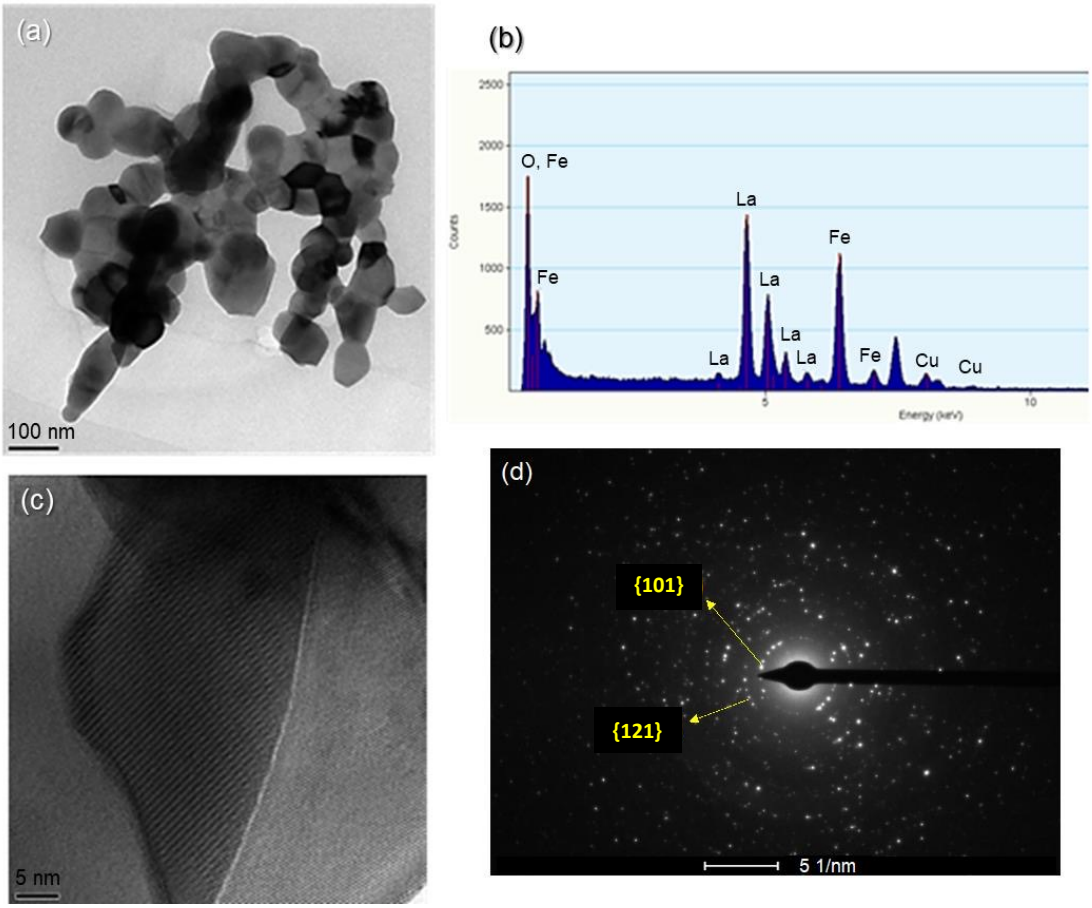

Figure 5.2 – (a) TEM micrograph, (b) EDS spectrum, (c) HRTEM image, and (d) SAED pattern obtained for the LCuFO perovskite.

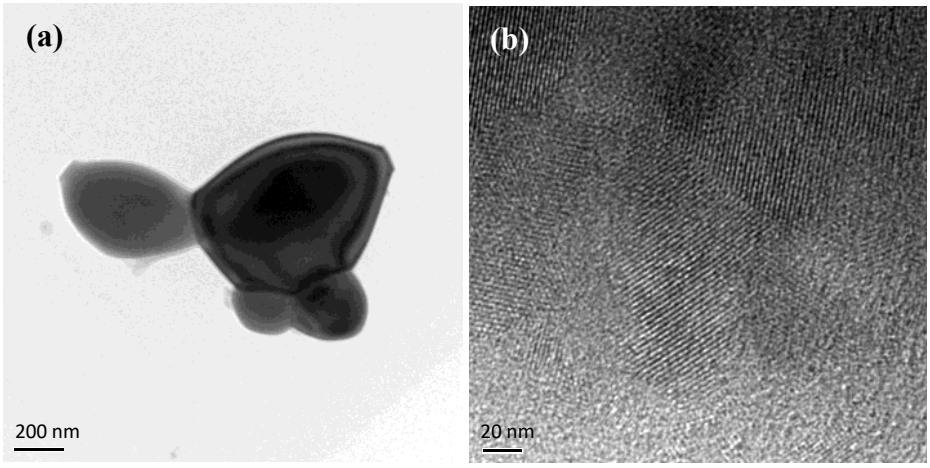

Figure 5.3 – (a) TEM micrograph, (b) HRTEM image obtained for the LFO perovskite.

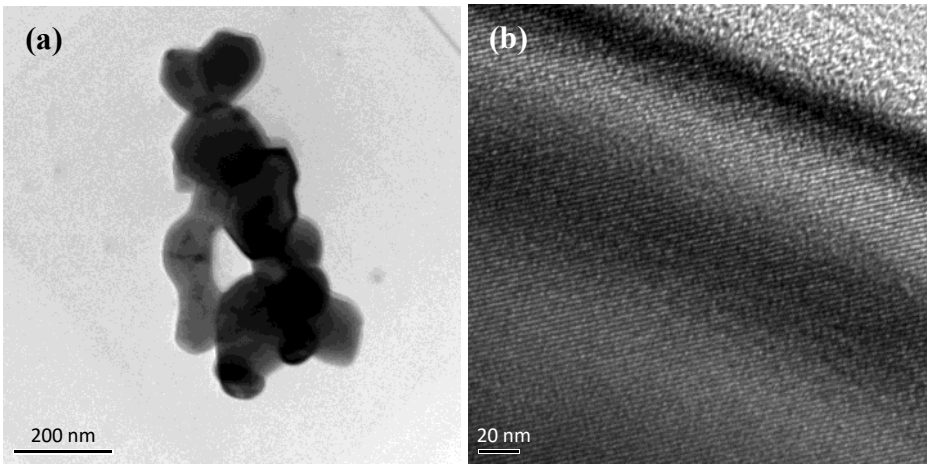

Figure 5.4 – (a) TEM micrograph, (b) HRTEM image obtained for the LCoO perovskite.

XPS analyses were performed to investigate the surface chemical composition of the perovskites prepared in this work. The high-resolution La 3d spectra of all samples (Fig. 5.5-5.8a) showed two doublets in the range of 830-837 eV and 850- 857 eV, corresponding to $La_{5/2}$ and $La_{3/2}$, respectively. The spin-orbit splitting difference in the La core level is approximately 16.7 eV, indicating a 3+ valence state for La (HAMMAD et al., 2023; LIN; CHEN; LIN, 2017). The slight shift in binding energy may be attributed to the incorporation of different elements into the perovskite lattice, resulting in changes in the electronic density around the core element (HAMMAD et al., 2023). Figs. 5.5b and 5.6b show the high-resolution spectra of Fe 2p for LFO and LCuFO, respectively. The peaks observed at 710-712

eV and 722- 725 eV are attributed to Fe $2p_{3/2}$ and Fe $2p_{1/2}$, respectively, with a shake-up satellite peak at 719 eV. This indicates that both perovskites contain Fe^{3+} species (LEONEL et al., 2021). Figs. 5.6c and 5.7b display the high-resolution spectra of Cu 2p for LCuFO and LCuO, respectively. The peaks centered at 934 eV and 953 eV are characteristic of Cu $2p_{3/2}$ and Cu $2p_{1/2}$, respectively. These results, combined with the three shake-up satellite peaks observed at 940-945 eV and 962 eV, strongly suggest the presence of Cu^{2+} species (GAO et al., 2023; LI et al., 2022).

The presence of a mixed oxidation state of Co^{2+} and Co^{3+} surface ions for LCoO is indicated by the Co 2p spectrum shown in Fig. 5.8b. The peaks at 779 eV and 795 eV correspond to the Co $2p_{3/2}$ and Co $2p_{1/2}$ orbitals of Co^{3+} species, with a binding energy difference of 15.2 eV. Peaks centered at 781 eV and 796 eV correspond to the Co 2p3/2 and Co 2p1/2 orbitals of Co^{2+} species (LI et al., 2022; LIN; CHEN; LIN, 2017).

The substitution of the B-site transition metal in the LFO lattice can introduce a charge imbalance, disrupting charge neutrality. It is plausible to expect either a change in the valence state of the transition metal or the formation of oxygen vacancies (O_v) to restore the charge balance. Since the valence state of Fe remained trivalent, it can be assumed that a higher concentration of O_v was formed (RAO et al., 2022). To investigate the formation of these species, we examined the high-resolution XPS spectrum of O 1s (Figs. 5.5c, 5.6d, 5.7c, and 5.8c). This spectrum can be resolved into two main peaks: one in the range of 528-530 eV, attributed to lattice oxygen (O_{lat}), and the other in the range of 530-532 eV, associated with adsorbed oxygen (O_{ads}) (ZHU et al., 2014). The O_{ads}/O_{lat} ratio of the areas shown in Table 5.1 is indicative of the surface oxygen vacancy concentration. Replacing Fe^{3+} with other transition metal species such as Cu^{2+} and Co^{2+} resulted in an increased O_V concentration, thereby compensating for the lack of positive charges within the perovskite lattice. Fig. 5.9 shows the comparison between both O_{lat} and O_{ads} in each studied perovskite.

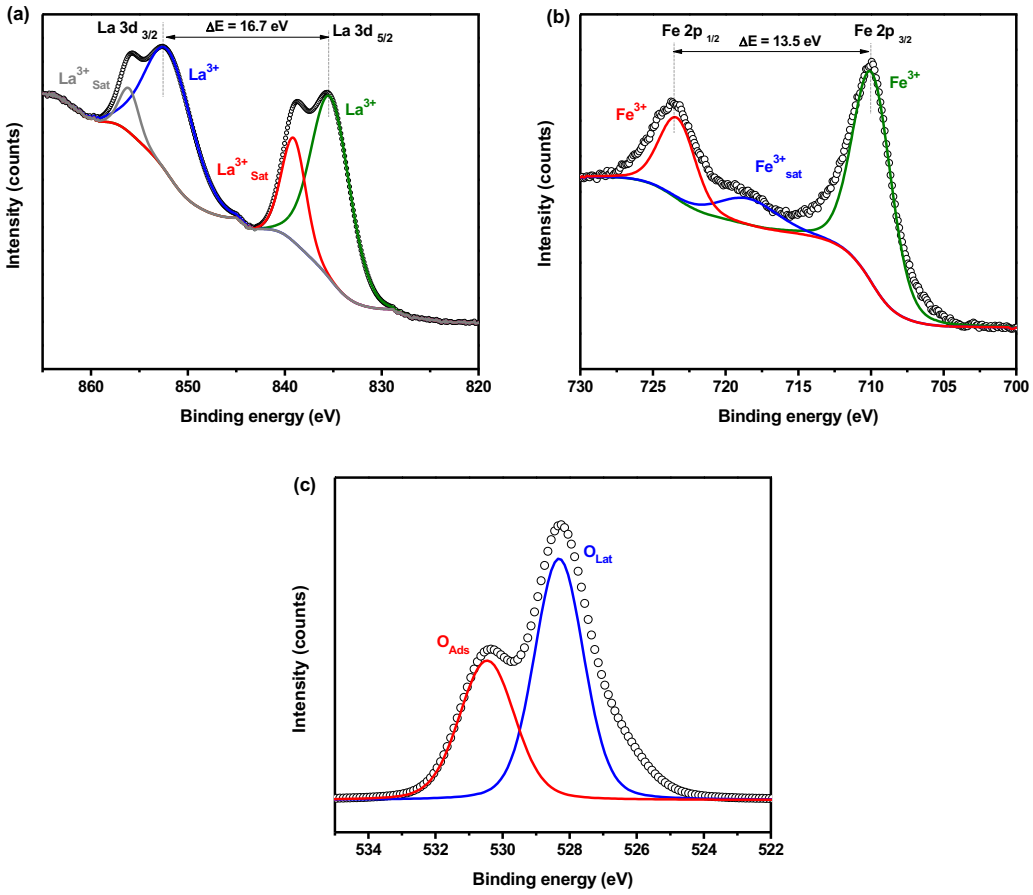

Figure 5.5 – XPS spectra of (a) La 3d, (b) Fe 2p, and (c) O 1s for LFO perovskite.

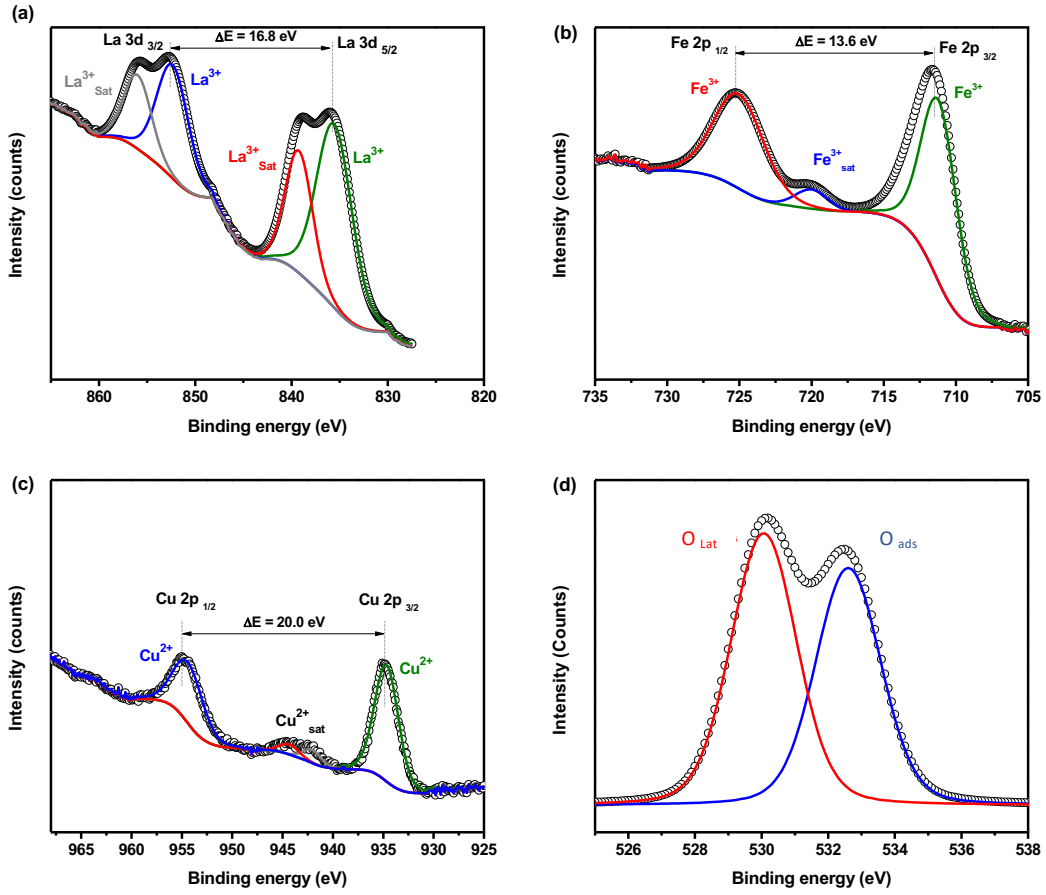

Figure 5.6 – XPS spectra of (a) La 3d, (b) Fe 2p, (c) Cu 2p, and (d) O 1s for LCuFO perovskite.

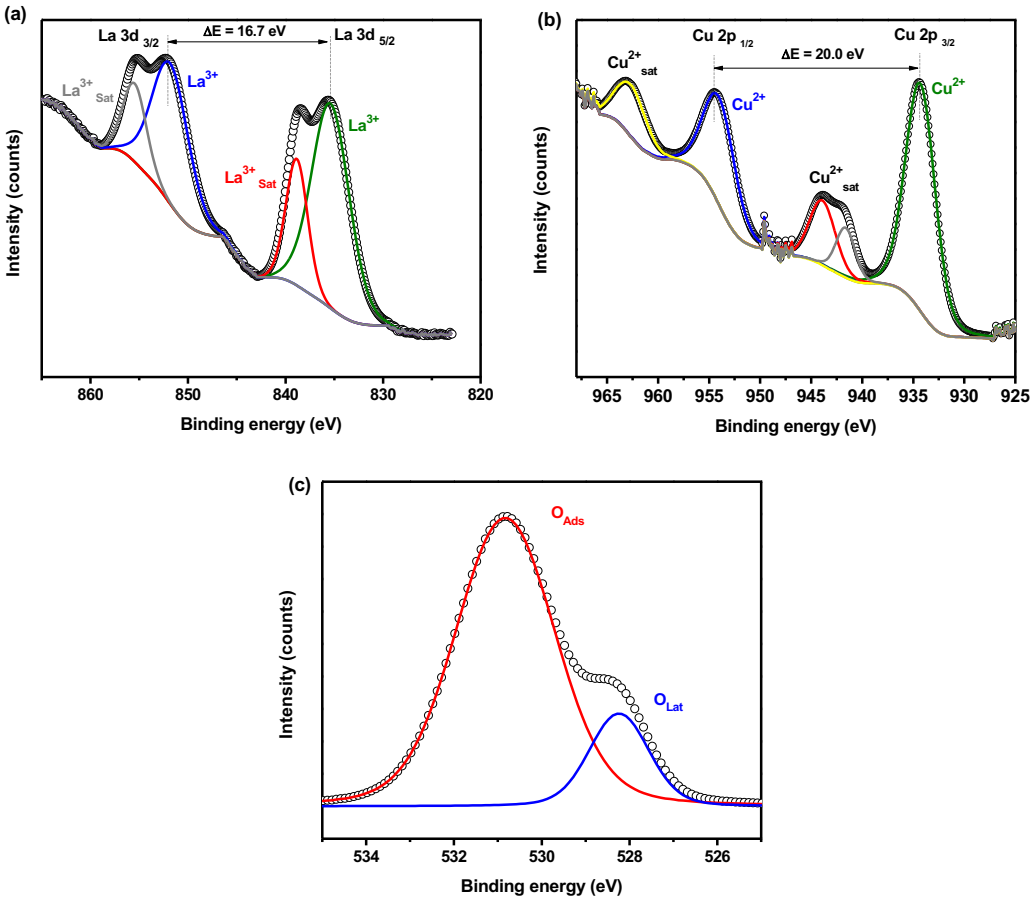

Figure 5.7 – XPS spectra of (a) La 3d, (b) Cu 2p, and (c) O 1s for LCuO perovskite.

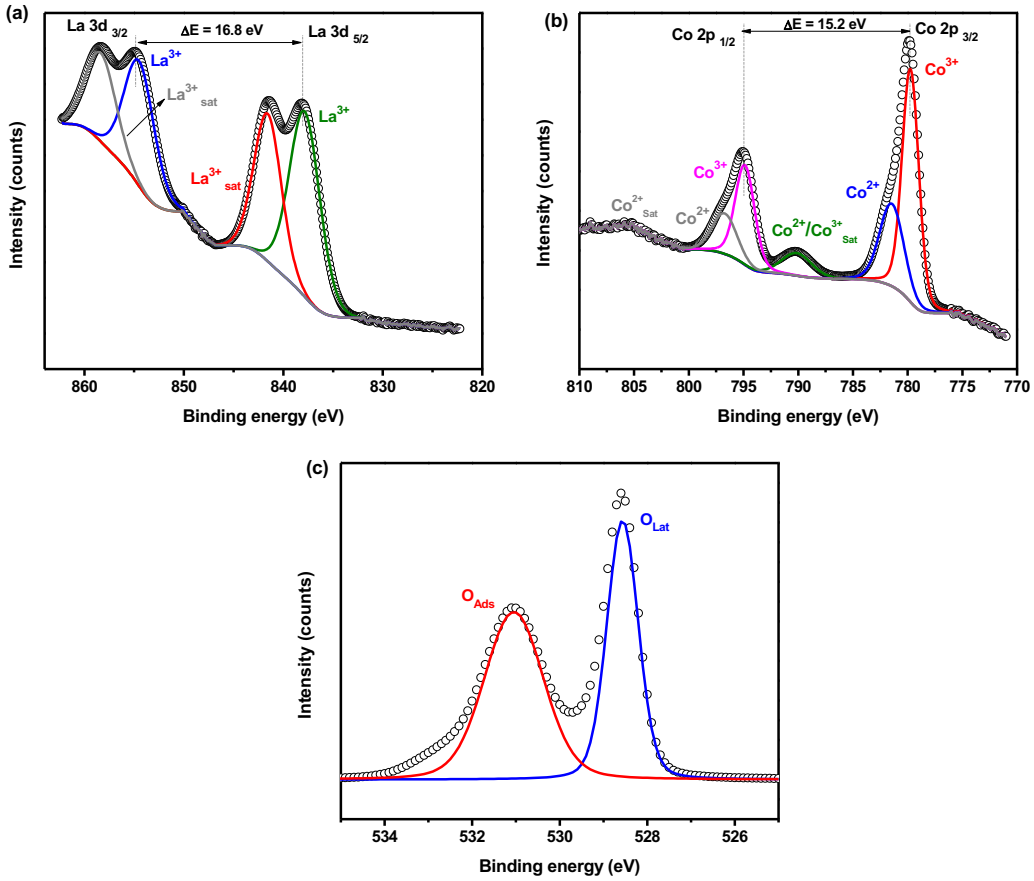

Figure 5.8 – XPS spectra of (a) La 3d, (b) Co 2p, and (c) O 1s for LCoO perovskite.

Table 5.1 – Ratio of adsorbed (O_{ads}) to lattice oxygen (O_{latt}) species, measured after the deconvolution of the XPS spectra.

Sample	O_{ads}/O_{latt} ratio
LFO	0.65
LCuO	5.20
LCuFO	0.86
LCoO	1.24

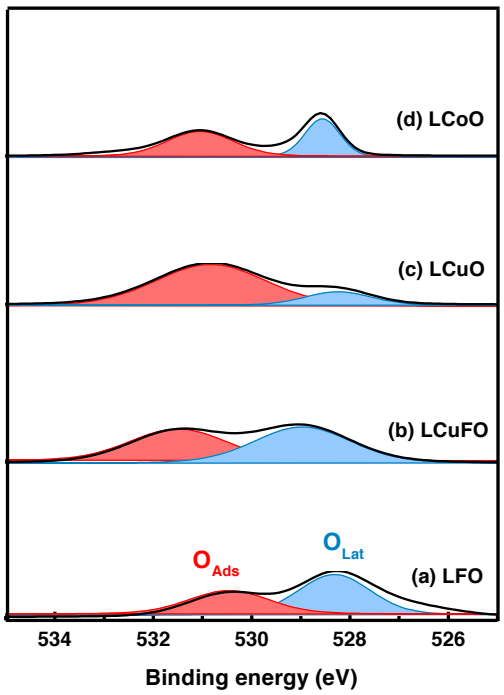

Figure 5.9 – O 1s spectra for (a) LFO, (b) LCuFO, (c) LCuO, and (d) LCoO.

Fourier Transform Infrared Spectroscopy (FTIR) is extensively used to determine functional groups present in the materials. Fig. 5.10 shows the FTIR spectra of all studied samples. The absorption bands observed from 700 cm^{-1} to 400 cm^{-1} have been attributed to vibrational modes of inorganic species present in the crystal lattice. Especially for perovskite oxides, these absorption bands are considered to be their main absorption bands. The absence of bands in the spectral range of 4000-800 cm^{-1} indicates the thorough removal of residues associated with synthesis precursors, such as nitrates and CA, during the calcination process. For LFO, the absorption bands between 650 cm^{-1} and 500 cm^{-1} are attributed to the asymmetric stretching vibration of Fe-O bonds from FeO_6 octahedra (ATEIA; HASSAN; ABDELMAKSOUD, 2021; RAJI et al., 2020). A comparison of the spectrum of LFO with that of LCuFO shows that the characteristic stretching modes do not change significantly with Cu doping, probably due to the low amount of this element in the latter. In contrast, LCuO showed two distinct absorption bands at 500 cm^{-1} and 680 cm^{-1} assigned to the stretching mode of Cu-O and La-O bonds from orthorhombic La_2CuO_4 (DHARMADHIKARI; NIKAM; ATHAWALE, 2014; SUKUMAR et al., 2018). It is worth remembering that such a phase was also observed by XRD (Fig. 5.1b). The bands at about 590 cm^{-1}, 530 cm^{-1}, and 400 cm^{-1} observed in the spectrum of LaCoO are attributed to the stretching mode of Co-O bonds from CoO_6 octahedra (HAMMAD et al., 2023; SUKUMAR et al., 2018; YAO et al., 2020).

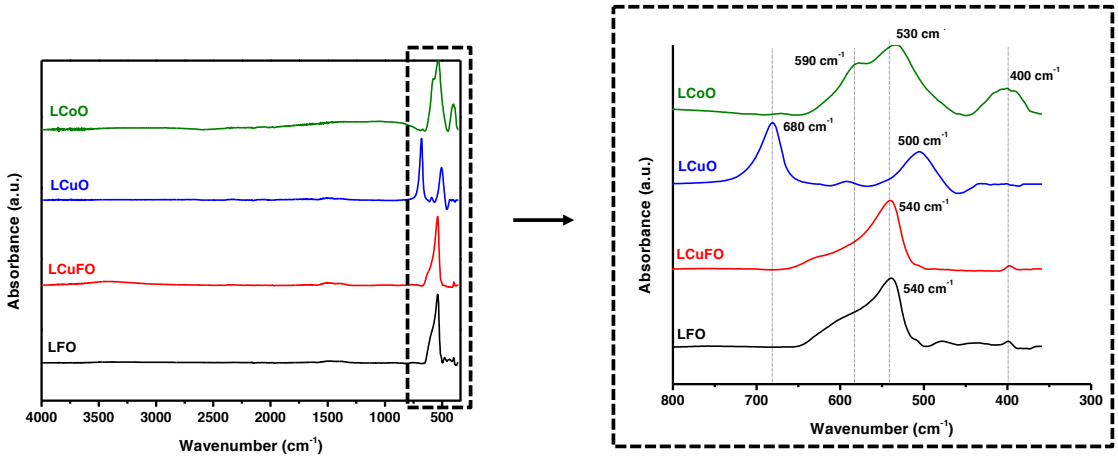

Figure 5.10 – Wide-range and detailed region of the FTIR spectra.

Fig. 5.11 presents N_2 sorption isotherms of the La-based perovskites. According to the International Union of Pure and Applied Chemistry (IUPAC) guidelines, these curves exhibit Type II isotherms, a classification typically associated with macroporous solids (THOMMES et al., 2015). The perovskites prepared in this study have low specific surface areas, less than 7 $m^2.g^{-1}$, as shown in Table 5.2. This property can be detrimental to catalytic performance, as catalysis relies on interfacial interactions between active sites and reactant molecules for optimal efficiency.

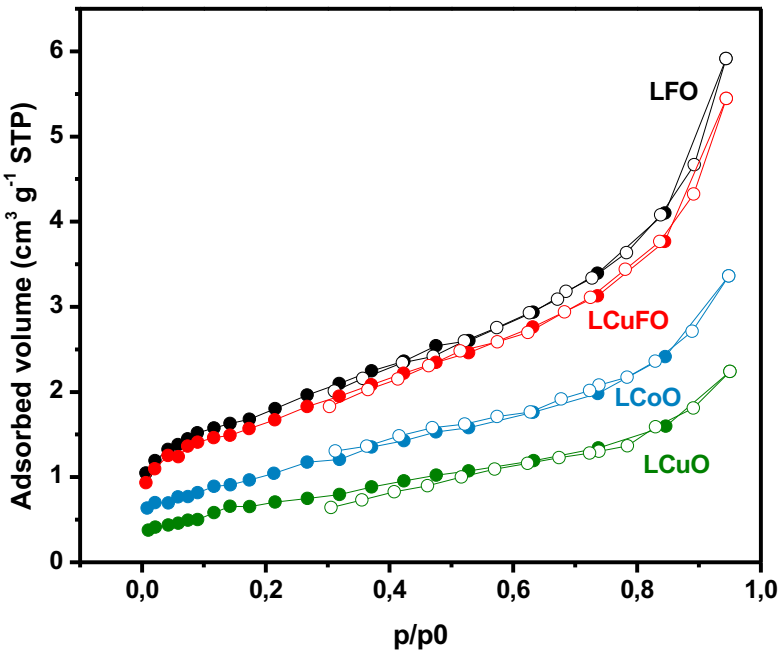

Figure 5.11 – N_2 sorption isotherms for $LaBO_3$ perovskites.

Table 5.2 – BET surface area evaluated for the LBO_3 perovskites.

Sample	SSA $_{BET}$ ($m^2.g^{-1}$)
LFO	6.3
LCuO	2.5
LCuFO	5.9
LCoO	3.9

5.1.2. Catalytic behavior of $LaBO_3$ perovskites

Perovskite-based metal oxides have attracted attention as promising heterogeneous catalysts for chemical oxidation processes. This is due to their high in harsh environments, the stable oxidation states of their transition metals, and the improved oxygen mobility within their crystal lattice (LIN; CHEN; LIN, 2017). Previous studies have shown that the catalytic behavior of ABO_3 perovskites is strongly related to the nature of the B-site. Therefore, the replacement of Fe in LFO by other multiple redox species such as Cu, Co, Cr, and Mn can dramatically affect the catalytic activity of the resulting material (PHAN et al., 2018). As a proof of concept, we evaluated the catalytic performance of the prepared perovskites in Fenton-like reactions for the degradation of methylene blue (MB). The effects of B-site transition metal, initial pH, catalyst-to-pollutant dosing ratio, concentration, and type of oxidant were studied to identify optimal parameters for the catalytic reactions.

As shown in Fig. 5.12a, LCuFO and LCuO exhibited superior catalytic activities compared to LFO. This result can be attributed to the efficient generation of free radicals by the decomposition of H_2O_2. Traditionally, the Fenton process using LFO materials involves the decomposition of H_2O_2 to produce hydroxyl radicals ($HO^{\bullet}$) through a catalytic reaction with ferrous ions (Fe^{2+}) present in the catalyst structure, as outlined in Eq. 5.1. Subsequently, the Fe^{2+} species can be regenerated through the reduction of the formed Fe^{3+} ions by the excess of H_2O_2, producing hydroperoxyl radicals ($HOO^{\bullet}$) *via* Fenton-like reactions (Eq. 5.2). These free radicals then interact with pollutant molecules, converting them into organic radicals that undergo a series of oxidation reactions, ideally resulting in the formation of H_2O and CO_2 (Eq. 5.3) (HUSSAIN; ANEGGI; GOI, 2021; PHAN et al., 2018).

$$\text{Catalyst-Fe(II)} + H_2O_2 \rightarrow \text{Catalyst-Fe(III)} + OH^{\bullet} + OH^{-} \qquad k = 40\text{-}80\ M^{-1}s^{-1} \qquad (5.1)$$

$$\text{Catalyst-Fe(III)} + H_2O_2 \rightarrow \text{Catalyst-Fe(II)} + HOO^{\bullet} + H^{+} \qquad k = 0.001\text{-}0.01 M^{-1}s^{-1} \qquad (5.2)$$

$$RH + HO^{\bullet} / HOO^{\bullet} \rightarrow H_2O + R^{\bullet} \rightarrow \text{Oxidation} \qquad (5.3)$$

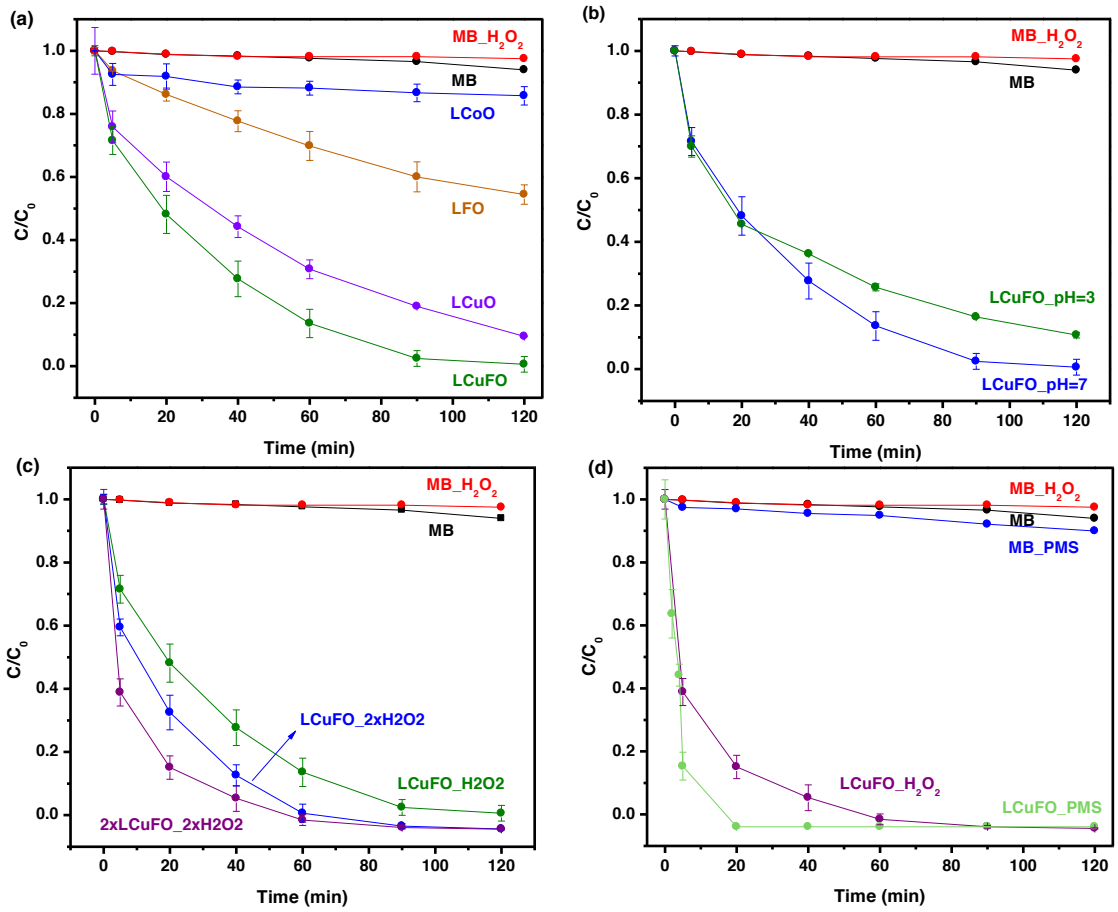

Figure 5.12 – (a) Catalytic behavior of different La-based perovskites in the presence of H_2O_2 as an oxidizing agent. Reaction conditions include a solution pH of 7, a catalyst/MB dosing ratio set as 666, and an H_2O_2 concentration of 1.4 mg.mL^{-1}. (b) Catalytic behavior of LCuFO at different pH values. The reaction conditions involve a catalyst/MB dosing ratio of 666 and an H_2O_2 concentration of 1.4 mg.mL^{-1}. (c) Catalytic behavior of LCuFO examined under varying H_2O_2 concentrations and catalyst/MB dosing ratio. Reaction conditions include a pH of 7, catalyst/MB dosing ratio of either 666 or 1333, and H_2O_2 concentrations of either 1.4 mg.mL^{-1} or 2.8 mg.mL^{-1}. (d) Catalytic behavior of LCuFO in the presence of various oxidants. The reaction conditions consist

of a pH of 7, a catalyst/MB dosing ratio (in the presence of H_2O_2) set at 1333, a catalyst/MB dosing ratio (in the presence of PMS) of 666, an H_2O_2 concentration of 2.8 mg.mL^{-1}, and a PMS concentration of 0.06 mg.mL^{-1}. All tests were conducted at room temperature.

Similarly, other metal transition ions with multiple redox states, such as Co and Cu, can also decompose H_2O_2 into free radicals *via* conventional Fenton-like pathways as described below (BOKARE; CHOI, 2014b; MAO et al., 2018; PHAN et al., 2018; XIE et al., 2022). Cu has similar redox properties to Fe in terms of reactivity towards H_2O_2. Both the monovalent and divalent oxidation states of Cu react with H_2O_2 (Eqs. 5.4 and 5.5), similar to the reaction systems involving Fe^{2+}/H_2O_2 and Fe^{3+}/H_2O_2 reaction systems. However, the capacity of Cu interconversion (Cu^+ /Cu^{2+}) is superior, resulting in a highly efficient redox cycle and increased production of free radicals (BOKARE; CHOI, 2014b; HUSSAIN; ANEGGI; GOI, 2021).

$$\text{Catalyst-Cu(I)} + H_2O_2 \rightarrow \text{Catalyst-Cu(II)} + HO^{\bullet} + OH^- \qquad k = 1 \times 10^4 \ M^{-1}s^{-1} \quad (5.4)$$

$$\text{Catalyst-Cu(II)} + H_2O_2 \rightarrow \text{Catalyst-Cu(I)} + HOO^{\bullet} + H^+ \qquad k = 5 \times 10^2 \ M^{-1}s^{-1} \quad (5.5)$$

Another factor contributing to the improved performance of LCuO is the charge imbalance of the lattice created by the substitution of Fe^{3+} with Cu^{2+}. To preserve the electrical neutrality of the lattice, the formation of O_v can take place, thereby creating additional active sites for adsorption and catalysis. This phenomenon significantly contributes to the effective decomposition of H_2O_2 (THOMAS; DIONYSIOU; PILLAI, 2021; XIE et al., 2022).

Additionally, it is important to note that LCuFO showed the highest catalytic performance among the catalysts examined in the study. This behavior can be related to the synergistic interaction of transition metals where the presence of Cu favors the reduction of Fe^{3+} to Fe^{2+} by H_2O_2 (Eqs. 5.6-5.8). As a result, this performance enhancement significantly accelerates the decomposition rate of H_2O_2 into free radicals (LE et al., 2020; PHAN et al., 2018). Conversely, LCoO exhibited the lowest catalytic activity, achieving only 10% MB removal within a 2h reaction time.

EPR measurements with DMPO were performed to identify the reactive species involved in the MB degradation. As shown in Fig. 5.13a(i), a weak EPR signal for DMPO-HO• adducts was observed in the presence of H_2O_2, justifying the low catalytic activity of LCoO. Additional catalytic tests were performed with LCuFO due to its improved catalytic behavior.

$$\text{Catalyst-Fe(III)} + e^- \rightarrow \text{Catalyst-Fe(II)} \quad (5.6)$$

$$\text{Catalyst-Cu(I)} \rightarrow \text{Catalyst-Cu(II)} + e^- \quad (5.7)$$

$$\text{Catalyst-Fe(III)} + \text{Catalyst-Cu(I)} \rightarrow \text{Catalyst-Fe(II)} + \text{Catalyst-Cu(II)} \quad (5.8)$$

Regarding the influence of the initial pH of the solution, Fig. 5.12b shows the MB degradation using solutions adjusted to pH = 3 and pH = 7. Notably, the efficiency of this process decreased as the pH was reduced from 7 to 3. This finding is consistent with the existing literature, which typically indicates higher efficiencies for Fe-based Fenton processes at pH values near 3, while Cu-loaded catalysts may exhibit superior performance over a wider pH range (5.5-9.5), particularly at near-neutral conditions (LIU et al., 2024).

Another critical factor affecting catalytic activity is the concentration of Fenton reactants. H_2O_2 plays a key role in determining the efficiency for HO• radical formation. Inadequate concentrations of H_2O_2 can lead to reduced radical production and consequently reduced pollutant oxidation. Conversely, an excessive concentration of H_2O_2 can induce a scavenging effect, minimizing the treatment efficiency (WANG et al., 2016). Similarly, the catalyst concentration should be optimized to ensure ideal radical production. Therefore, the effects of H_2O_2 dosage and LCuFO loading were also investigated. Thus, the oxidant concentration was increased from 1.4 $mg.mL^{-1}$ to 2.8 $mg.mL^{-1}$. As depicted in Fig. 5.12c, in evident that the degradation of MB showed higher efficiency with increasing concentration of H_2O_2 at constant catalyst dosage (as indicated by the blue and green curves), as expected. Likewise, catalytic efficiency was improved by increasing the catalyst dosage while keeping the oxidant concentration constant. The increase in catalytic efficiency in both cases is attributed to the generation of higher concentrations of free radicals, which play a critical role in the degradation of MB (LEONEL; MANSUR; MANSUR, 2021; YE et al., 2023).

The EPR measurements displayed in Fig. 5.13a(ii) and (iii) confirm that the intensity of the characteristic spectral line of the DMPO-HO• adducts (i.e., the quadruplet of the adduct with a peak intensity ratio of 1:2:2:1) increases with raising oxidant concentration (Fig. 5.13a(ii)) and both catalyst and oxidant concentrations (Fig.5.13a(iii)) (RAO et al., 2022).

To evaluate the effectiveness of the LCuFO catalyst in different catalytic processes, we introduced a new parameter by examining the type of oxidant. In this case, we used PMS as a precursor of sulfate radicals and defined sulfate-radical-based AOP. Fig. 5.12d shows the degradation of MB in the presence of either H_2O_2 (purple curve) or PMS (green curve). The catalytic performance was superior when PMS was used due to the formation of sulfate radicals. Under these conditions, almost all the MB content was degraded within the first 20 min of reaction. It is important to note that the catalyst/pollutant ratio and oxidant concentration were not kept identical for the two processes, but were determined from the literature values (RAO et al., 2018; SOLÍS; RIVAS; GIMENO, 2017). These findings reveal that the PMS-based process was more effective, achieving superior results with lower values for both catalyst/pollutant dosing ratio and oxidant dosage compared to the H_2O_2-based process (catalyst/MB dosing ratio = 666 *vs* 1333 and oxidant concentration = 0.06 mg.mL^{-1} *vs* 2.8 mg.mL^{-1}). Degradation kinetic studies were performed using the Langmuir-Hinshelwood (LH) kinetic model, which has been widely employed for describing heterogeneous catalytic processes (HAMMAD et al., 2023). This model is based on Eq. 5.9, where k_{app} (min^{-1}) is the apparent first-order rate constant, C_0 is the initial concentration of the pollutant, and C is the concentration of the pollutant at time t. The values inferred for k_{app} are given in Table 5.3.

$$\ln \frac{C}{C_0} = -k_{app}\, t \tag{5.9}$$

Table 5.3 – Reaction rate constant (k_{app}) for different perovskites and catalytic parameters.

Sample	k_{app} ($\times 10^{-3}$ min^{-1})	R^2
LFO_H_2O_2_pH7	9	0.995
LCuO_H_2O_2_pH7	18	0.984
LCoO_H_2O_2_pH7	0.6	0.980

LCuFO_H_2O_2_pH7	40	0.984
LCuFO_H_2O_2_pH3	16	0.943
LCuFO_2xH_2O_2_pH7	66	0.969
2xLCuFO_2xH_2O_2_pH7	124	0.983
LCuFO_PMS_pH7	249	0.891

These results validate the higher catalytic behavior of LaCuFO and its superior performance in PMS-based reactions where lower catalyst and oxidant doses are required to achieve significant degradation. The high efficacy of sulfate-based AOP can be attributed to several factors including the comparable or even higher oxidizing power and longer half-life than $SO_4^{\bullet-}$ compared to $^{\bullet}OH$ (ROJAS-CERVANTES; CASTILLEJOS, 2019; XIAO et al., 2020). Furthermore, when PMS is used as the oxidant, the degradation pathway can produce not only $SO_4^{\bullet-}$ radicals but also $HO^{\bullet}$ radicals (WANG et al., 2019), as shown in Eq. 5.10 (M represents a metal species) (ZHONG et al., 2023) and Fig.5.13a(iv). The identification of the sulfate radical through EPR spectra is still controversial. While some studies suggest that the six-line spectrum exhibited in Fig. 5.13a(iv) (green curve) is indicative of the DMPO-$SO_4^{\bullet-}$ adduct (HAMMAD et al., 2023; SHAO et al., 2023), others propose that this spectrum represents the product of DMPO oxidation by the presence of metal species (DAI et al., 2020; LONG et al., 2021). Wang and coworkers (WANG et al., 2020) correlate this spectrum with DMPO-X signals resulting from metal leaching in perovskite samples. However, such leaching is more pronounced under acidic conditions, at a pH typically around 2 (WANG et al., 2019). The weak signal of DMPO-$SO_4^{\bullet-}$ can be associated with the short-lived nature of the adducts in water ($t_{1/2}$ = 95 s), which are rapidly converted to DMPO- $HO^{\bullet}$ by nucleophilic substitution reactions (RAO et al., 2022).

To verify the stability of the LCuFO catalyst, XRD before and after catalytic reactions were performed. The perovskite after sulfate-based reaction tests were collected through centrifugation, dried at 80 ºC until the complete evaporation of water, and then heat-treated in air at 500 ºC for 2 h to remove impurities. As evidenced in Fig. 5.13b, there was no change in phase composition and crystalline structure, indicating the good stability of the catalyst.

$$HSO_5^- + Catalyst - M^n \rightarrow Catalyst - M^{n+1} + SO_4^{\cdot -} + HO^{\cdot} \quad (5.10)$$

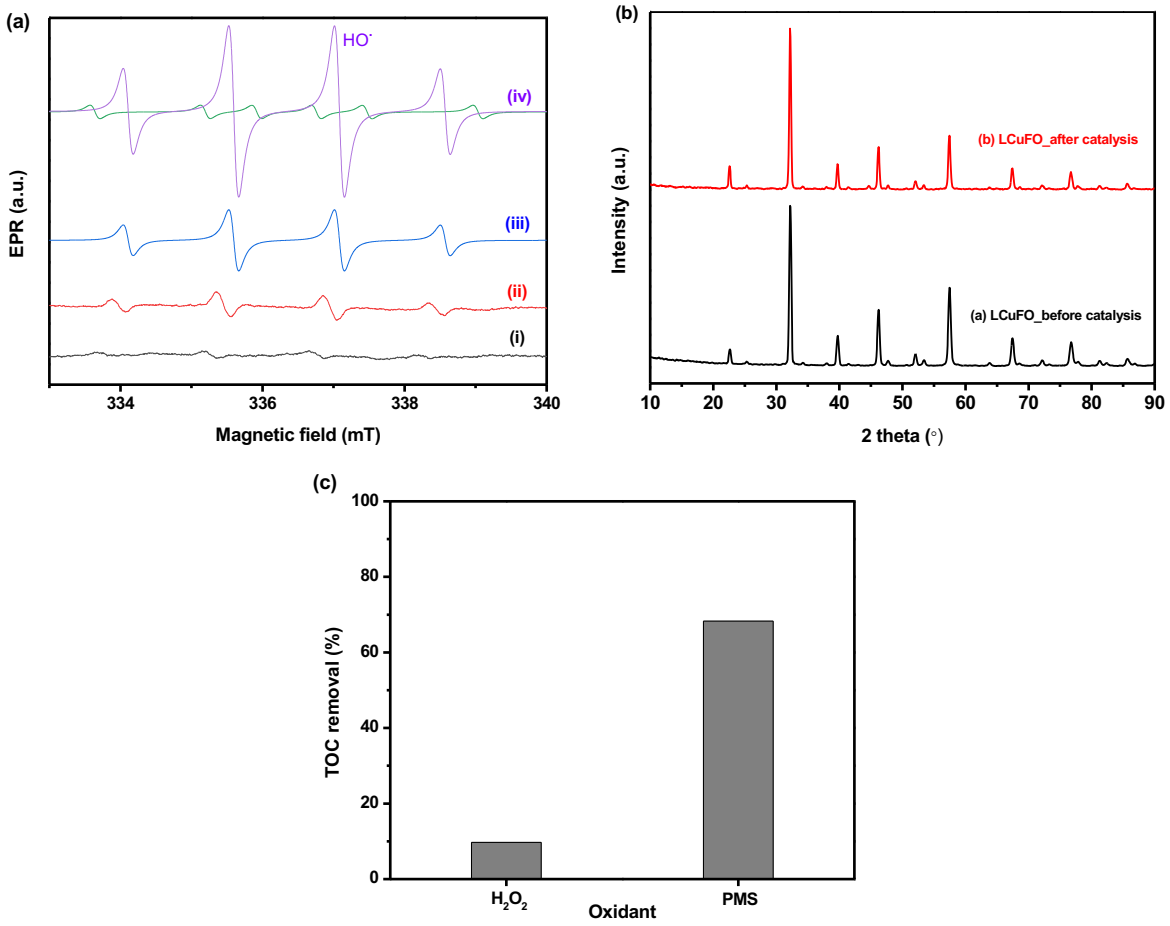

Figure 5.13 – (a) EPR spin-trapping experiments performed with DMPO in an aqueous solution containing: (i) LCoO and H_2O_2, (ii) LCuFO and 2 x H_2O_2, (iii) 2 x LCuFO and 2 x H_2O_2, (iv) LCuFO and PMS as a function of time. (b) TOC concentration in an MB solution assessed after the conclusion of catalytic reactions. (c) XRD of LCuFO before and after catalytic activity. Reaction conditions: pH = 7, catalyst/MB dosing ratio = 666, PMS concentration = 0.06 mg.mL^{-1}. All tests were conducted at room temperature.

It is important to highlight that the LCuFO perovskite prepared in this study exhibits significant catalytic capability despite its relatively low specific surface area (5.9 m^2.g^{-1}). In the study of Dong and coworkers (DONG et al., 2023), LCuFO prepared with bis (hexamethylene triamine penta (methylene phosphonic acid)) as a complexing agent was used to activate PMS for the degradation of biologically treated coking effluent. The removal efficiency (C/C_0) reached only about 0.3 within 30 min despite the higher surface area of the

material (10.8 $m^2.g^{-1}$). In contrast, under the same Cu content and pH conditions, our material achieved a C/C_0 of 0.2 within only 5 min. In addition, our study used a significantly lower concentration of PMS (0.06 $mg.mL^{-1}$ *vs.* 3.0 $mg.mL^{-1}$), providing a more sustainable approach. Guan and coworkers (GUAN et al., 2024) focused on the preparation of oxygen vacancy-enriched LCuFO perovskite using a Prussian blue metal-organic framework template. They reported a high bisphenol A degradation efficiency of 98% within 30 min. Their mesoporous perovskite, which had a Cu doping concentration similar to ours and a higher surface area (about 12 $m^2.g^{-1}$), required a higher concentration of PMS. In addition, their synthesis process involved the use of potassium ferrocyanide, which poses a higher environmental risk than the water-based method used in our study. In summary, our material shows excellent catalytic activity and offers more sustainable practical contributions compared to recent literature. Future improvements could be achieved through techniques such as nanocasting, which favors the synthesis of mesoporous perovskites with increased specific surface area (ALCAMAND et al., 2023).

To provide additional confirmation of MB degradation during the catalytic process, the mineralization rate was evaluated by TOC analysis. As shown in Fig. 5.13c, the TOC concentration was approximately 10% and 70% for LCuFO after catalytic tests performed for 120 min in the presence of H_2O_2 and PMS, respectively. This indicates that the mineralization rate for the Fenton-like process was lower compared to the PMS-based process. After 120 min of reaction, the transformation products in the Fenton-like process remained predominantly organic (GAO et al., 2020).

5.2. Mesoporous La-based perovskites

5.2.1. Structural and physicochemical characterization of SBA-16 and NO-MS templates

The SBA-16 formed template exhibited a small-angle X-ray diffractogram (Fig. 5.14a) with (100), (110), and (200) reflections, which are indicative of an ordered porous structure (ALCAMAND et al., 2023). The low relative intensities of the diffraction peaks originate from the high rate of wall thickness and pore size (STEVENS et al., 2006). Conversely, the X-ray diffractogram of NO-MS (Fig. 5.14b) did not exhibit any peak in the small-angle region, which evidenced a non-ordered porous structure.

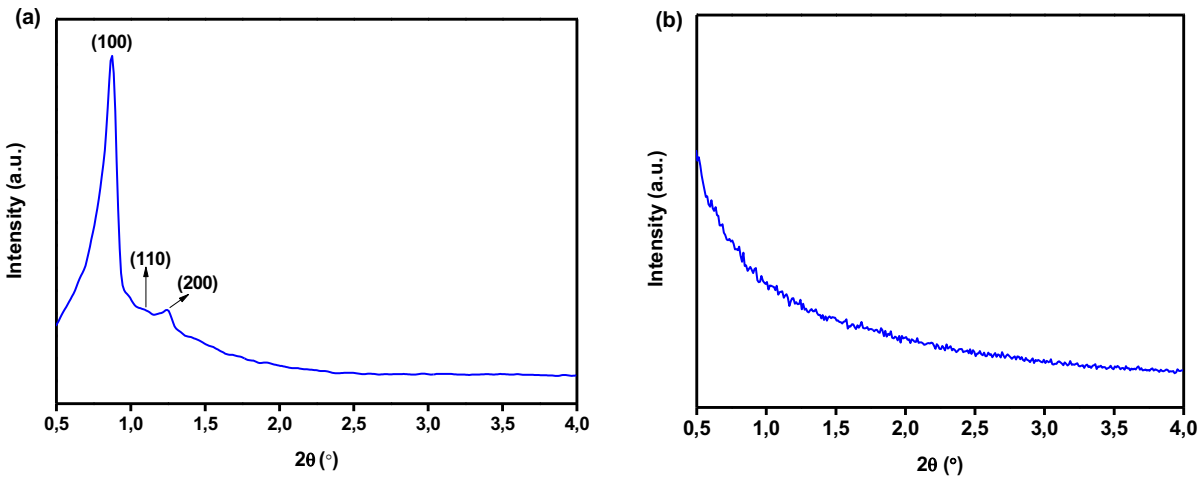

Figure 5.14 – Small-angle XRD pattern of (A) SBA-16 and (B) NO-MS.

Figure 5.15a exhibits a high-resolution TEM image of the SBA-16 template. An ordered pore network is observed in this image, which was previously confirmed by small-angle XRD. The EDS analysis was performed to evaluate the composition of the hard template. As expected, the EDS spectrum (Fig. 5.15b) confirmed the presence of Si and O. The signals attributed to Cu and C are associated with the carbon-coated copper grid used as the sample substrate. The SAED pattern in Fig. 5.15c displays an amorphous halo, confirming the amorphous nature of the silica sample.

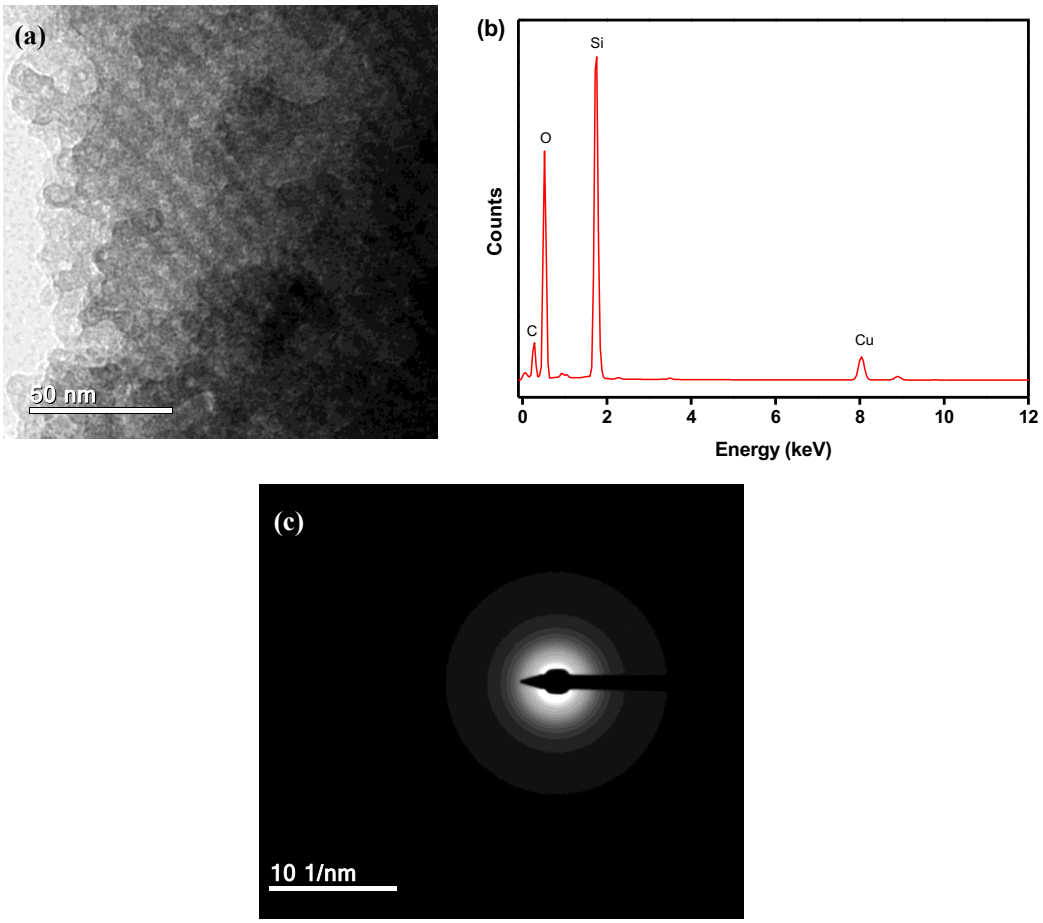

Figure 5.15 – (a) TEM micrograph, (b) EDS spectrum, and (c) SAED pattern of SBA-16.

Fig. 5.16 shows the FTIR spectra of SBA-16 and NO-MS samples. Absorption bands characteristic of silica were observed in both FTIR spectra. The bands at about 1060 cm^{-1} and 460 cm^{-1} correspond to asymmetric stretching and bending vibrations of Si-O-Si bonds. The adsorption bands around 800 cm^{-1} are also attributed to stretching vibrations of Si-O-Si bonds. One additional peak at 950 cm^{-1} was observed in the NO-MS sample, which could be attributed to the bending vibra0tion of surface Si-O bonds, *i.e.,* the non-bonding oxygen atoms of Si-OH (DHANESWARA et al., 2022; ESPERANZA ADROVER et al., 2020; HOUMARD et al., 2009; LU et al., 2020).

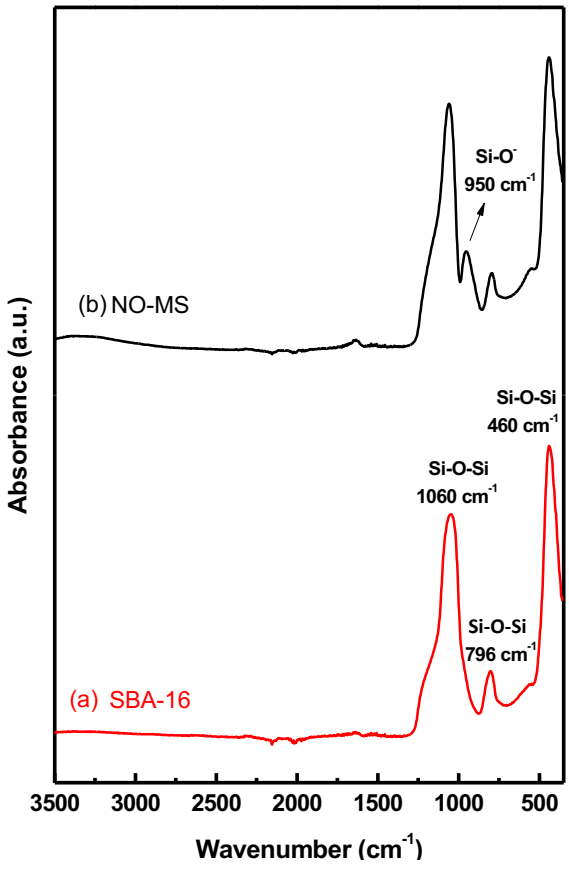

Figure 5.16 – FTIR curves of (a) SBA-16 and (b) NO-MS.

Fig. 5.17 presents N_2 sorption isotherms of SBA-16 template. According to the International Union of Pure and Applied Chemistry (IUPAC) guidelines, this curve exhibits Type IV isotherms with hysteresis loop, which is typically observed for mesoporous solids

(THOMMES et al., 2015). Capillary condensation occurred at relative pressures of 0.4-0.6. The specific surface area and pore volume were estimated at 555 $m^2.g^{-1}$ and 0.36 $cm^3.g^{-1}$, respectively.

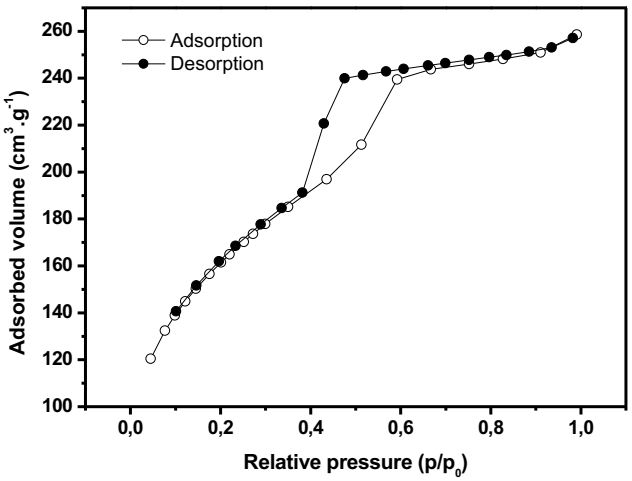

Figure 5.17 – N_2 sorption isotherm of SBA-16.

5.2.2. Structural and physicochemical characterization of LCuFO_SBA-16 perovskites

The wide-angle XRD pattern of LCuFO_SBA-16, depicted in Fig. 5.18b, shows the same peaks as LCuFO. This indicates that the nanocasting method used to introduce mesoporosity into the perovskite structure effectively preserved its composition and orthorhombic crystal structure (JCPDS #37-1493). On the other hand, the XRD pattern of LCuFO_NO-MS, depicted in Fig. 5.18c, did not reveal the presence of crystal phases. This result was expected considering that the conversion of infiltrated metal nitrate precursors to metal oxide nanoparticles occurs inside and outside the silica pore network. Thus, the lack of ordered pore structure restrains the formation of crystalline particles confined in porous hosts (SCHOLZ et al., 2017).

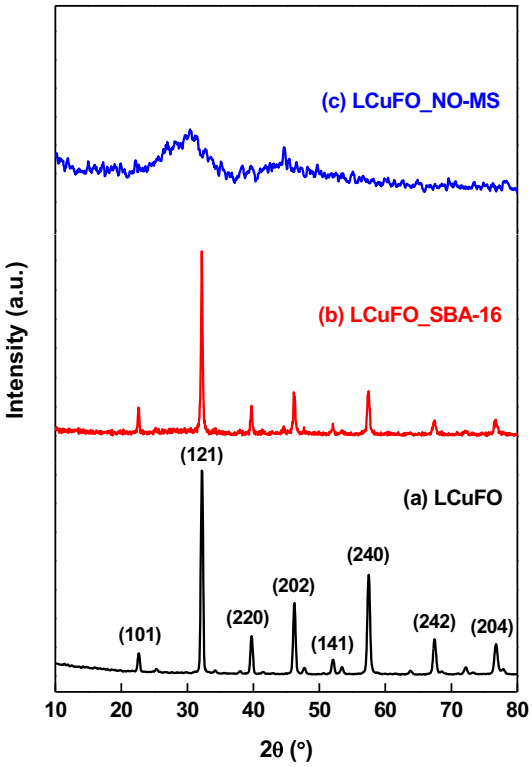

Figure 5.18 – XRD pattern of (a) LCuFO, (b) LCuFO_SBA-16, and (c) LCuFO_NO-MS.

Fig. 5.19a shows the TEM micrograph of LCuFO_SBA-16 revealing agglomerated particles with irregular morphology. As discussed earlier, these properties can be attributed to the heat treatment used to obtain perovskites by the citrate method, which involves calcination at 550 °C for 2 h followed by 750 °C for 6 h (ALCAMAND et al., 2022; ATEIA; HASSAN; ABDELMAKSOUD, 2021; ZHANG et al., 2023). EDS analysis confirmed the presence of La, Cu, Fe, and O (Fig. 5.19b). The presence of C and Ni is attributed to the Formvar Nickel grid used as the sample substrate, while the presence of Si is probably due to residual template material that was not completely removed during the NaOH wash. High-resolution TEM micrographs (Fig. 5.19c), reveal interference fringes, confirming the polycrystalline nature of the materials. The SAED pattern in Figs. 5.19d displays concentric ring patterns characteristic of Bragg diffraction. These rings correspond to the (101), (121), (220), (240), and (202) crystal planes, consistent with lanthanum ferrite perovskites (PHAN et al., 2018; RAO et al., 2018), as discussed earlier in the XRD analysis (Fig. 5.18).

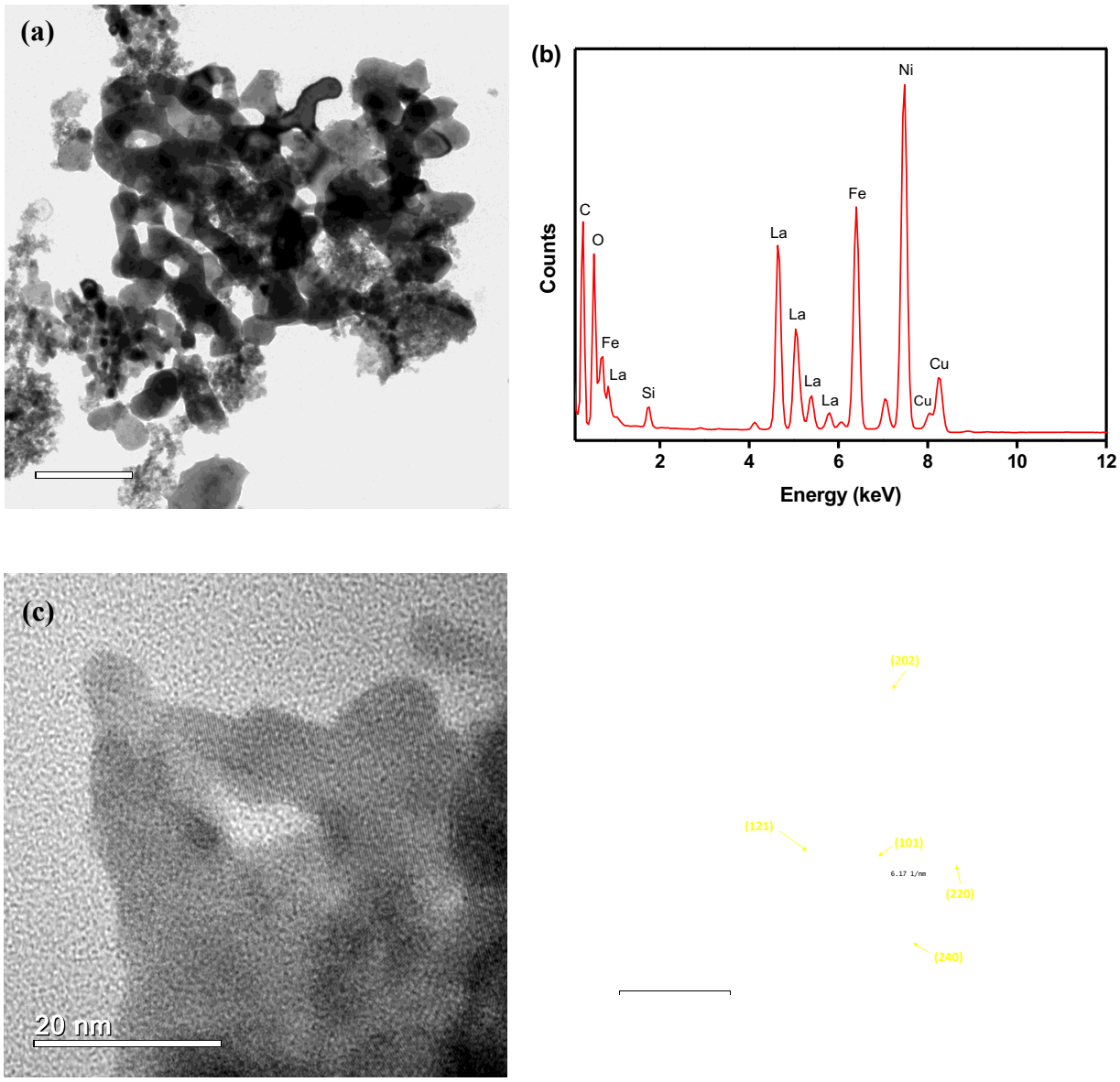

Figure 5.19 – (a) TEM micrograph, (b) EDS spectrum, (c) HRTEM image, and (d) SAED pattern of LCuFO_SBA-16.

N_2 sorption analysis (Fig. 5.20a) revealed Type II isotherms for LCuFO, indicative of macroporous structures, and Type IV isotherms with hysteresis loops for LCuFO_SBA-16, characteristic of mesoporous materials (THOMMES et al., 2015). The SSA of LCuFO_SBA-16 increased ninefold compared to LCuFO due to its mesoporous structure (57 m^2g^{-1} *vs.* 6 m^2g^{-1}). Comparison of the FTIR spectra for LCuFO and LCuFO_SBA-16 (Fig. 5.20b) shows an absorption band at 540 cm^{-1} characteristic of metal-O stretching modes attributed to orthorhombic $LaFeO_3$ (LEONEL et al., 2024). However, a distinct band at 956 cm^{-1},

attributed to non-bonding oxygen atoms in Si-OH groups, is observed in LCuFO_SBA-16, probably due to residual template material as indicated by EDS analysis (Fig. 5.19b).

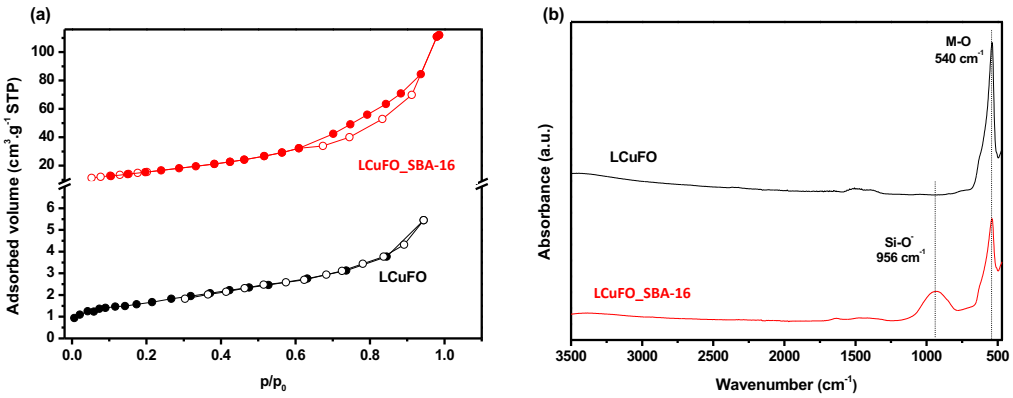

Figure 5.20 – (a) N_2 sorption isotherms and (b) FTIR spectra of LCuFO and LCuFO_SBA-16.

5.2.3. Catalytic behavior of LCuFO_SBA-16 perovskites

The catalytic performance of the mesoporous perovskites was initially evaluated for the degradation of MB through Fenton reactions. To evidence the influence of the mesoporous structure on the adsorption and catalytic behavior of LCuFO_SBA-16 perovskites, reaction conditions applied in this new material include pH of 7, catalyst concentration of 2 $mg.mL^{-1}$, H_2O_2 concentration of 1.4 $mg.mL^{-1}$, and MB concentration of 3 $\mu g.mL^{-1}$.

The adsorption performance was observed within 60 min, time to reach the adsorption-desorption equilibrium. Figure 5.21a shows that the adsorption effect of LCuFO on MB removal was negligible. Conversely, Fig. 5.21b evidenced a significant MB removal (approximately 40%) in only 5 min, indicating the better adsorption ability of LCuFO_SBA-16, presumably due to the higher surface area of the catalyst, which means a larger number of adsorption sites (LEONEL et al., 2021). After achieving the equilibrium state, the oxidant was added to the systems, and the catalytic performance was evaluated within the next 2 h. Although both systems exhibited a similar reaction rate constant ($k_{app} \sim 0.04\ min^{-1}$) based on the Langmuir-Hinshelwood (LH) kinetic model, the MB degradation process was faster for the LCuFO_SBA-16 catalyst, considering the association of adsorption and catalytic processes.

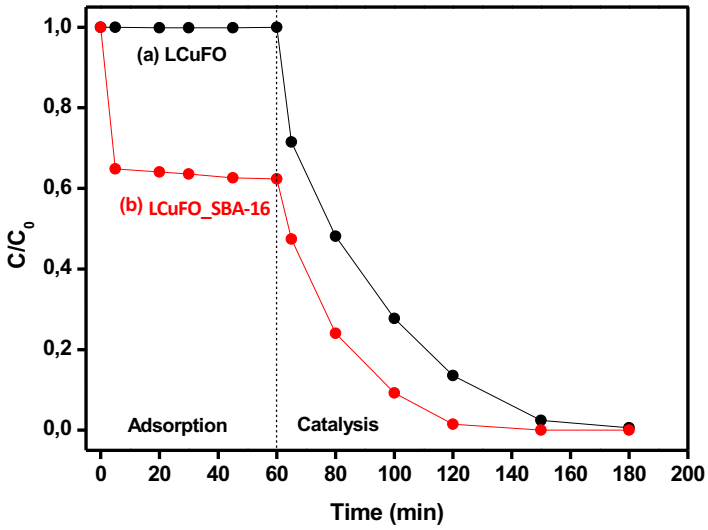

Figure 5.21 – Adsorption and catalytic behavior of porous (LCuFO_SBA-16) and non-porous (LCuFO) perovskites in the presence of H_2O_2 as an oxidizing agent for MB removal. Reaction conditions include a solution pH of 7, a catalyst/MB dosing ratio of 666, and an H_2O_2 concentration of 1.4 mg.mL^{-1}. The tests were conducted at room temperature.

To demonstrate that the catalyst is effective for the degradation of different classes of pollutants, we have chosen a pharmaceutical to study the catalytic activity of LCuFO_SBA-16 perovskite. Doxorubicin (DOX) belongs to a class of cytotoxic drugs commonly used for cancer chemotherapy. Because of its widespread use, water pollution by this emerging contaminant has become a considerable environmental issue (ALTHUMAYRI et al., 2023).

As previously performed for MB removal, This evaluation involved two sequential steps: first, the adsorption of DOX on the catalysts, followed by a catalytic reaction in the presence of PMS as the oxidant. The reaction was conducted under controlled conditions, including a pH of 6.5 ± 0.2, a catalyst concentration of 0.08 mg.mL^{-1}, a PMS concentration of 3.1 mg.mL^{-1}, and a DOX concentration of 0.1 mg.mL^{-1} (SU et al., 2024). The adsorption of DOX on both catalysts was minimal, with less than 2% adsorption observed for LCuFO and approximately 4% for LCuFO_SBA-16 after 4 h (Fig. 5.22). While a higher SSA can enhance the adsorption process, it is crucial to consider other factors, such as the availability of reactive sites (LI et al., 2023b). The low catalyst-to-DOX dosage ratio employed in this study led to rapid saturation of the active sites, which limited significant removal of DOX. Upon reaching equilibrium, PMS was introduced into the system. After 2 h of reaction, LCuFO achieved

approximately 40% degradation of DOX, while LCuFO_SBA-16 degraded 98% of DOX in only 5 min. The removal efficiency (C/C_0) of the mesoporous perovskite demonstrated its remarkable catalytic activity despite the ultra-low-dose catalyst (less than 0.1 $mg.mL^{-1}$).

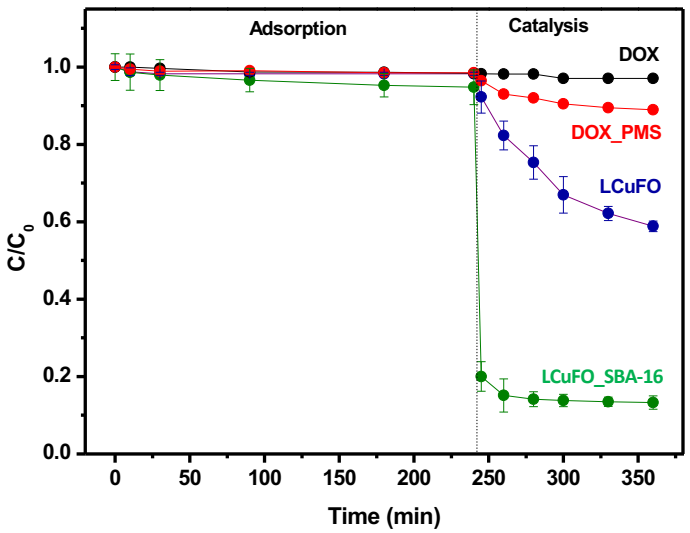

Figure 5.22 – Adsorption and catalytic behavior of porous (LCuFO_SBA-16) and non-porous (LCuFO) perovskites in the presence of PMS as an oxidizing agent for DOX removal. Reaction conditions include a solution pH of 6.5, a catalyst/DOX dosing ratio of 0.8, and a PMS concentration of 3.1 $mg.mL^{-1}$. The tests were conducted at room temperature.

6. CONCLUSION

In this work, we have successfully employed an environmentally friendly aqueous process based on the conventional citrate method for the synthesis of high-purity La-based perovskites. These perovskites were characterized for their structural and physicochemical properties, which were then correlated with their catalytic behavior. Microscopic analysis revealed the formation of agglomerated particles with irregular morphology, consistent with the synthesis route used. While the high-temperature range (550-750 °C) and prolonged calcination time (2-6 h) resulted in particle coalescence, they also contributed to the preparation of perovskites with enhanced crystallinity, as demonstrated by XRD analysis. FTIR analyses demonstrated the effectiveness of the heat treatment in removing by-products such as citric acid and nitrates, as no characteristic organic bands were observed in any spectrum. The substitution of Fe^{3+} at the B-site with Cu^{2+} or Co^{2+} had a dramatic effect not only on the crystal lattice but also on the catalytic behavior. The co-doping of La-based perovskites with Cu and Fe resulted in samples with improved catalytic performance, reaching a reaction rate constant as high as 0.25 min^{-1}, despite their low surface area (5.9 $m^2.g^{-1}$). This improved catalytic behavior was attributed to a synergy of factors, including oxygen vacancy formation and redox properties. Regarding the oxidation processes used to test the catalytic properties, sulfate-based reactions showed a superior ability to mineralize the organic dye MB. Mesoporous LCuFO perovskites were also successfully synthesized using the nanocasting method with SBA-16 silica as a hard template. The introduction of mesoporosity significantly increased the specific surface area of the perovskite, which improved its adsorption and catalytic activity. Remarkably, the removal efficiency of DOX from the aqueous phase reached 98% within only 5 min of reaction by using the mesoporous catalyst, demonstrating a much higher catalytic performance compared to previously reported results. Given these results, LCuFO perovskite appears to be a promising material for water remediation. In addition to investigating various compositions of La-based perovskites and elucidating the catalysis mechanism, this study introduces a novel aspect by prioritizing environmental safety through the utilization of an organic solvent-free synthesis method. This approach not only amplifies the significance of this study but also ensures the sustainability of the production process. These contributions enhance the comprehension of perovskite catalysts and their potential applications in environmental remediation.

CONCLUSÃO

Neste trabalho, perovskitas à base de La foram produzidas com base em uma abordagem ecologicamente sustentável utilizando o método citrato convencional sem o emprego de solventes orgânicos. Essas perovskitas foram caracterizadas para avaliar suas propriedades estruturais e físico-químicas, que foram então correlacionadas ao seu comportamento catalítico. A análise microscópica revelou a formação de partículas aglomeradas com morfologia irregular, resultado consistente com a rota de síntese empregada, que faz uso de altas temperaturas (550-750 °C) e tempos prolongados de calcinação (2-6 h). No entanto essas condições favoreceram a obtenção de perovskitas com alta cristalinidade, conforme demonstrado pela análise de XRD. As análises de FTIR demonstraram a eficácia do tratamento térmico na remoção de subprodutos como ácido cítrico e nitratos, uma vez que nenhuma banda orgânica característica foi observada em nenhum espectro. A substituição de Fe^{3+} no sítio B por Cu^{2+} ou Co^{2+} apresentou um efeito significativo não apenas na estrutura cristalina, mas também no comportamento catalítico do material. A co-dopagem com Cu e Fe resultou em amostras com melhores desempenhos catalíticos, observando-se uma alta constante de taxa de reação (0.25 m^{-1}), comparada as outras condições estudadas, apesar de sua baixa área de superfície (5,9 $m^2.g^{-1}$). Esse comportamento catalítico foi atribuído a sinergia de fatores como a formação de vacâncias de oxigênio e propriedades redox dos elementos constituintes. Em relação aos processos de oxidação utilizados para testar as propriedades catalíticas, as reações baseadas na geração de radical sulfato mostraram uma capacidade superior de mineralizar o corante orgânico (MB). Perovskitas do tipo LCuFO mesoporosas também foram sintetizadas com sucesso pelo método de *nanocasting* que utilizou a sílica SBA-16 como *template.* A produção de mesoporosidade nas perovskitas aumentou significativamente sua área superficial específica, o que por sua vez melhorou a sua adsorção e atividade catalítica. A eficiência de remoção de DOX da fase aquosa atingiu 98% em apenas 5 min de reação, demonstrando um desempenho catalítico muito maior em comparação com resultados reportados na literatura. Além de investigar várias composições de perovskitas à base de La e elucidar os mecanismos de catálise, este estudo introduziu um novo aspecto ao priorizar a utilização de rotas de síntese livres de solventes orgânicos, garantindo a sustentabilidade do processo de produção e potencializando aplicações desses materiais em tratamento de águas residuais.

7. SUGGESTIONS FOR FUTURE WORK

- Investigate catalyst reusability and its efficiency after successive cycles by measuring metal leaching from the reaction product solution using Inductively Coupled Plasma (ICP) spectroscopic analysis;
- Examine the influence of the LaCuFO/DOX loading ratio and the pH solution to optimize both adsorption and catalytic processes;
- Examine the influence of the Cu doping content within LFO perovskites on their physicochemical and catalytic properties;
- Evaluate the reaction product solution after catalytic experiments through HPLC (High-Performance Liquid Chromatograph) to identify the possibly remaining organic sub-products;
- Investigate the influence of different parameters of perovskite impregnation on the mesoporous structure of SBA-16, such as SBA-16/perovskite loading ratio and NaOH concentration;
- Evaluate the photocatalytic activity of LCuFO_SBA-16;
- Assessment of the *in vitro* toxicity of the LBO_3 perovskites by MTT experiments with different catalyst concentrations and exposure times.

8. ORIGINAL CONTRIBUTIONS TO KNOWLEDGE

- Published papers

LEONEL, A. G; ALCAMAND, H.A; DINIZ, M. P. V; GASTELOIS, P. L; KRAMBROCK, K; HOUMARD, M; NUNES, E. H. M. Influence of B-site cation on the structural and catalytic properties of $LaBO_3$ (B = Fe, Cu, Co, or Fe + Cu) perovskites. **Journal of Alloys and Compounds**, v. 1005, p. 176260, 2024.

LEONEL, A.G; MANSUR, A. A. P; MANSUR, H. S. Advanced Functional Nanostructures based on Magnetic Iron Oxide Nanomaterials for Water Remediation: A Review. **Water Research**, v. 190, p. 116693, 2021.

LEONEL. A. G; MANSUR, A. A. P; CARVALHO, S. M; OUTON, L. E. F; ARDISSON, J. D; KRAMBROCK, K; MANSUR, H. S. Tunable magnetothermal properties of cobalt-doped magnetite-carboxymethylcellulose ferrofluids: smart nanoplatforms for potential magnetic hyperthermia applications in cancer therapy. **Nanoscale Advances**, v. 4, p. 1-18, 2021.

- Published book chapters

LEONEL, A. G ; MANSUR, A. A. P; SANDER, H. S. Magnetic Iron Oxide Nanoparticles and Nanohybrids for Advanced Water Treatment Technology. In: Springer Nature Switzerland AG 2022. Thomas, S; Nochehdehi, A. R (eds.). Handbook of Magnetic Hybrid Nanoalloys and their Nanocomposites. 1ª ed. Cham-Switzerland: Springer Nature - Cham, 2022, v. 1, p. 1103-1125.

LEONEL, A. G ; MANSUR, A. A. P; SANDER, H. S. Nanotoxicity and Environmental Risks of Magnetic Iron Oxide Nanoparticles and Nanohybrids. In: Springer Nature Switzerland AG 2022. Thomas, S; Nochehdehi, A. R (eds.). Handbook of Magnetic Hybrid Nanoalloys and their Nanocomposites. 1ª ed. Cham-Switzerland: Springer Nature - Cham, 2022, v. 1, p. 1225-1250.

- Submitted papers

LEONEL, A. G; DE SOUZA, M. G; SOARES, D; HOUMARD, M; NUNES, E. H. M. Preparation of mesoporous Cu-doped $LaFeO_3$ perovskites with high catalytic efficiency for doxorubicin removal. **Material Letters**, submitted in November 4th, 2024

9. REFERENCES

AFZAL, S. et al. Efficiency and mechanism of high surface area mesoporous nanocast NC-$LaCoO_3$ for activating peroxymonosulfate to degrade atrazine in water. **Separation and Purification Technology**, v. 354, p. 128823, 2025.

ALCAMAND, H. et al. Environmentally friendly synthesis of imine using $LaMnO_3$ as a catalyst under continuous flow conditions. **Materials Letters**, v. 316, 2022.

ALCAMAND, H. A. et al. Synthesis, characterization, and use of nanocast $LaMnO_3$ perovskites in the catalytic production of imine by the gas-phase oxidative coupling of benzyl alcohol to aniline. **Catalysis Communications**, v. 175, 2023.

ALPHA; AWWA; WEF. **Standard Methods for examination of water and wastewater Encyclopedia of Meat Sciences**, 2012.

ALTHUMAYRI, K. et al. Effective Adsorption and Removal of Doxorubicin from Aqueous Solutions Using Mesostructured Silica Nanospheres: Box-Behnken Design Optimization and Adsorption Performance Evaluation. **ACS Omega**, v. 8, p. 14144–14159, 2023.

ALVAREZ, P. J. J. et al. Emerging opportunities for nanotechnology to enhance water security. **Nature Nanotechnology**, v. 13, p. 634–641, 2018.

ARIMI, M. M. M. et al. Recent trends in applications of advanced oxidation processes (AOPs) in bioenergy production: Review. **Renewable and Sustainable Energy Reviews**, v. 121, p. 1–18, 2020.

ATEIA, E. E.; HASSAN, H. I.; ABDELMAKSOUD, E. M. K. Structural and Magnetic Tuning of - LaFeO3 Orthoferrite Substituted Different Rare Earth Elements to Optimize Their Technological Applications. **Journal of Inorganic and Organometallic Polymers and Materials**, v. 31, p. 1713–1725, 2021.

BABUPONNUSAMI, A.; MUTHUKUMAR, K. A review on Fenton and improvements to the Fenton process for wastewater treatment. **Journal of Environmental Chemical Engineering**, v. 2, p. 557–572, 2014.

BACHA, A. U. R. et al. Environmental application of perovskite material for organic pollutant-enriched wastewater treatment. **Coordination Chemistry Reviews**, v. 495, p. 215378, 2023.

BARTEL, C. J. et al. New tolerance factor to predict the stability of perovskite oxides

and halides. **Science Advances**, v. 5, p. 1–10, 2019.

BELLO, M. M.; RAMAN, A. A. A.; ASGHAR, A. A review on approaches for addressing the limitations of Fenton oxidation for recalcitrant wastewater treatment. **Process Safety and Environmental Protection**, v. 126, p. 119–140, 2019.

BOKARE, A. D.; CHOI, W. Review of iron-free Fenton-like systems for activing H_2O_2 in advanced oxidation processes. **Journal of Hazardous Materials**, v. 275, p. 121–135, 2014a.

BOKARE, A. D.; CHOI, W. Review of iron-free Fenton-like systems for activating H_2O_2 in advanced oxidation processes. **Journal of Hazardous Materials**, v. 275, p. 121–135, 2014b.

CARRASCO-DÍAZ, M. R. et al. Efficient removal of paracetamol using $LaCu_{1-x}M_xO_3$ (M = Mn, Ti) perovskites as heterogeneous Fenton-like catalysts. **Chemical Engineering Journal**, v. 304, p. 408–418, 2016.

CHEN, Z. et al. A review on the application of perovskite catalysts for sulfate radical-based advanced oxidation processes. **Journal of Industrial and Engineering Chemistry**, 2024.

CORSI, I. et al. Ecofriendly nanotechnologies and nanomaterials for environmental applications: Key issue and consensus recommendations for sustainable and ecosafe nanoremediation. **Ecotoxicology and Environmental Safety**, v. 154, p. 237–244, 2018.

DAI, P. et al. Kinetics and mechanism study of H-acid degradation by peroxymonosulfate activation with Co_3O_4-Fe_2O_3/Al_2O_3. **Korean Journal of Chemical Engineering**, p. 961–968, 2020.

DEL ÁLAMO, A. C. et al. Fenton-like catalyst based on a reticulated porous perovskite material: Activity and stability for the on-site removal of pharmaceutical micropollutans in a hospital wastewater. **Chemical Engineering Journal**, v. 401, p. 126113, 2020.

DHANESWARA, D. et al. Spherical SBA-16 particles synthesized from rice husk ash and corn cob ash for efficient organic dye adsorbent. **Journal of Cleaner Production**, v. 357, p. 131974, 2022.

DHARMADHIKARI, D. V; NIKAM, S. K.; ATHAWALE, A. A. Template free hydrothermal synthesis and gas sensing application of lanthanum cuprate (La_2CuO_4): Effect of precursors on phase formation and morphology. **Journal of Alloys and Compounds**, v. 590, p. 486–493, 2014.

DIAS, J. A. et al. Lanthanum-Based Perovskites for Catalytic Oxygen Evolution Reaction. p. 3173–3192, 2020.

DONG, Z. et al. Efficient treatment of recalcitrant biologically treated coking wastewater using Cu-doped $LaFeO_3$/peroxymonosulfate activator: Performance evaluation and response surface methodology modeling. **Colloids and Surfaces A: Physicochemical and Engineering Aspects**, v. 679, p. 132602, 2023.

ESPERANZA ADROVER, M. et al. Synthesis and characterization of mesoporous SBA-15 and SBA-16 as carriers to improve albendazole dissolution rate. **Saudi Pharmaceutical Journal**, v. 28, p. 15–24, 2020.

FALCÓN, H. et al. Bulk and surface structures and their relevance in CO oxidation. **Applied Catalysis B: Environmental**, v. 26, p. 131–142, 2000.

FATIMAH, S. et al. How to Calculate Crystallite Size from X-Ray Diffraction (XRD) using Scherrer Method. **ASEAN Journal of Science and Engineering**, v. 2, p. 65–76, 2022.

FERROUDJ, N. et al. Increasing the efficiency of magnetic heterogeneous Fenton catalysts with a simple halogen visible lamp. **Journal of Photochemistry and Photobiology A: Chemistry**, v. 338, p. 85–95, 2017.

GAO, L. et al. Effect of dissolved organic matters and inorganic ions on TiO_2 photocatalysis of diclofenac: mechanistic study and degradation pathways. **Environmental Science and Pollution Research**, v. 27, p. 2044–2053, 2020.

GAO, P. et al. Activation of peroxymonosulfate by La_2CuO_4 perovskite for synergistic removal of Microcystis aeruginosa and microcystin-LR in harmful algal bloom impacted water. **Applied Catalysis B: Environmental**, v. 328, p. 122511, 2023.

GOMES, A. L. M. et al. Facile sol–gel synthesis of silica sorbents for the removal of organic pollutants from aqueous media. **Journal of Materials Research and Technology**, v. 15, p. 4580–4594, 2021.

GONÇALVES, B. S. et al. Effect of the carbon loading on the structural and photocatalytic properties of reduced graphene oxide-TiO_2 nanocomposites prepared by hydrothermal synthesis. **Journal of Materials Research and Technology**, v. 8, p. 6262–6274, 2019.

GUAN, Y. et al. Cu-doped oxygen-rich vacancy MOFs derived perovskite for enhanced mineralization of refractory organics through synergistic non-radical species effects.

Separation and Purification Technology, v. 335, p. 126072, 2024.

HAMMAD, M. et al. Synthesis of novel $LaCoO_3$ / graphene catalysts as highly efficient peroxymonosulfate activator for the degradation of organic pollutants. **Chemical Engineering Journal**, v. 454, p. 139900, 2023.

HODGES, B. C.; CATES, E. L.; KIM, J. Challenges and prospects of advanced oxidation water treatment processes using catalytic nanomaterials. **Nature Nanotechnology**, v. 13, p. 642–650, 2018.

HOUMARD, M. et al. Surface Science Water and oil wettability of hybrid organic – inorganic titanate – silicate thin films deposited via a sol – gel route. **Surface Science**, v. 603, p. 2698–2707, 2009.

HUANG, L. et al. Research progresses on the application of perovskite in adsorption and photocatalytic removal of water pollutants. **Journal of Hazardous Materials**, v. 442, p. 130024, 2023.

HUSSAIN, S.; ANEGGI, E.; GOI, D. Catalytic activity of metals in heterogeneous Fenton - like oxidation of wastewater contaminants:a review. **Environmental Chemistry Letters**, v. 19, p. 2405–2424, 2021.

HWANG, J. et al. Perovskite in catalysis and electrocatalysis. **Science**, v. 358, p. 751–756, 2017.

IBRAHIM, I. et al. Water treatment by perovskite materials and their applications : A comprehensive review. **Journal of Industrial and Engineering Chemistry**, 2024.

JUENGCHAREONPOON, K.; WANICHPONGPAN, P.; BOONAMNUAYVITAYA, V. Graphene oxide and carboxymethylcellulose film modified by citric acid for antibiotic removal. **Journal of Environmental Chemical Engineering**, v. 9, p. 104637, 2021.

KALITA, E.; BARUAH, J. Environmental remediation. In: **Colloidal Metal Oxide Nanoparticles**. [s.l.] Elsevier Inc., 2020. p. 525–576.

KUCHARCZYK, B. et al. Physicochemical Properties of $LaFeO_3$ Perovskite Prepared by Various Methods and Its Activity in the Oxidation of Hydrocarbons. **Industrial and Engineering Chemistry Research**, v. 59, p. 16603–16613, 2020.

KUMAR, A.; KUMAR, A.; KRISHNAN, V. Perovskite Oxide Based Materials for Energy and Environment-Oriented Photocatalysis. **ACS Catalysis**, v. 10, p. 10253–10315, 2020.

KUMAR, D. et al. Synthesis Techniques and Applications of Perovskite Materials. In: **Perovskite Materials, Devices and Integration**. [s.l: s.n.]. p. 1–19.

LE, V. T. et al. Cu / Fe_3O_4 @ carboxylate-rich carbon composite: One-pot synthesis , characterization , adsorption and photo-Fenton catalytic activities. **Materials Research Bulletin**, v. 129, p. 110913, 2020.

LEONEL, A. G. et al. Tunable magnetothermal properties of cobalt-doped magnetite – carboxymethylcellulose magnetic hyperthermia applications in cancer therapy. **Nanoscale Advances**, v. 3, p. 1029–1046, 2021.

LEONEL, A. G. et al. Influence of B-site cation on the structural and catalytic properties of $LaBO_3$ (B = Fe, Cu, Co, or Fe + Cu) perovskites. **Journal of Alloys and Compounds**, v. 1005, p. 176260, 2024.

LEONEL, A. G.; MANSUR, A. A. P.; MANSUR, H. S. Advanced Functional Nanostructures based on Magnetic Iron Oxide Nanomaterials for Water Remediation: A Review. **Water Research**, v. 190, p. 116693, 2021.

LI, H. et al. Perovskite catalysts with different dimensionalities for environmental and energy applications: A review. **Separation and Purification Technology**, v. 307, p. 122716, 2023a.

LI, M. et al. Green and Efficient Al-Doped $LaFe_xA_{l1-x}O_3$ Perovskite Oxide for Enhanced Phosphate Adsorption with Creation of Oxygen Vacancies. **ACS Applied Materials and Interfaces**, v. 15, p. 16942–16952, 2023b.

LI, Y. et al. Oxygen-vacancy abundant electrospun Co-doped Ruddlesden-Popper perovskite catalysts for peroxymonosulfate activation and Rhodamine B degradation. **Journal of Cleaner Production**, v. 380, n. P2, p. 135117, 2022.

LIN, K. A.; CHEN, Y.; LIN, Y. $LaMO_3$ perovskites (M = Co , Cu , Fe and Ni) as heterogeneous catalysts for activating peroxymonosulfate in water. **Chemical Engineering Science**, v. 160, p. 96–105, 2017.

LIN, N. et al. Critical review of perovskite-based materials in advanced oxidation system for wastewater treatment: Design, applications and mechanisms. **Journal of Hazardous Materials**, v. 424, p. 127637, 2022.

LIU, Y. et al. Progress in copper-based supported heterogeneous electro-Fenton catalysts. **Chemical Engineering Journal**, v. 486, p. 150217, 2024.

LONG, Y. et al. Sulfur-containing iron nanocomposites confined in S/N co-doped

carbon for catalytic peroxymonosulfate oxidation of organic pollutants: Low iron leaching, degradation mechanism and intermediates. **Chemical Engineering Journal**, p. 126499, 2021.

LU, C. et al. Utilization of iron tailings to prepare high-surface area mesoporous silica materials. **Science of the Total Environment**, v. 736, p. 139483, 2020.

LU, F.; ASTRUC, D. Nanocatalysts and other nanomaterials for water remediation from organic pollutants. **Coordination Chemistry Reviews**, v. 408, p. 1–31, 2020.

MAMBA, G. et al. Heterogeneous advanced oxidation processes over stoichiometric ABO_3 perovskite nanostructures. **Materials Today Nano**, v. 18, p. 100184, 2022.

MAO, J. et al. Enhanced heterogeneous Fenton-like activity by Cu-doped $BiFeO_3$ perovskite for degradation of organic pollutants. **Environmental Science Engineering**, v. 12, p. 2–11, 2018.

MIAO, J. et al. Boosting performance of lanthanide magnetism perovskite for advanced oxidation through lattice doping with catalytically inert element. **Chemical Engineering Journal**, v. 355, p. 721–730, 2019.

MIRZAEI, A. et al. Removal of pharmaceuticals from water by homo/heterogonous Fenton-type processes-a review. **Chemosphere**, v. 174, p. 665–688, 2017.

MOTA, T. L. R. et al. Influence of the synthesis parameters on the mesoporous structure and adsorption behavior of silica xerogels fabricated by sol–gel technique. **Journal of Sol-Gel Science and Technology**, v. 92, p. 681–694, 2019.

PARWAIZ, S.; KHAN, M. M. Perovskites and perovskite-based heterostructures for photocatalytic energy and environmental applications. **Journal of Environmental Chemical Engineering**, v. 12, p. 113175, 2024.

PHAN, N. T. T. et al. Journal of Industrial and Engineering Chemistry Heterogeneous photo-Fenton degradation of organics using highly efficient Cu-doped $LaFeO_3$ under visible light. **Journal of Industrial and Engineering Chemistry**, v. 61, p. 53–64, 2018.

PIDBURTNYI, M. et al. A Review on Perovskite-Type $LaFeO_3$ Based Electrodes for CO_2 Reduction in Solid Oxide Electrolysis Cells: Current Understanding of Structure-Functional Property Relationships. **Chemistry of Materials**, v. 33, p. 4249–4268, 2021.

RAJI, R. K. et al. Conventional synthesis of perovskite structured $LaTi_xFe_{1-x}O_3$: A comprehensive evaluation on phase formation , opto-magnetic , and dielectrical

properties. **International Journal of Materials Research**, v. 112, p. 753, 2020.

RAO, Y. et al. Heterogeneous activation of peroxymonosulfate by $LaFeO_3$ for diclofenac degradation: DFT-assisted mechanistic study and degradation pathways. **Chemical Engineering Journal**, v. 352, p. 601–611, 2018.

RAO, Y. et al. Enhanced peroxymonosulfate activation by Cu-doped $LaFeO_3$ with rich oxygen vacancies: Compound-specific mechanisms. **Chemical Engineering Journal**, v. 435, n. January, 2022.

RODRIGUEZ-NARVAEZ, O. M. et al. Treatment technologies for emerging contaminants in water: A review. **Chemical Engineering Journal**, v. 323, p. 361–380, 2017.

ROJAS-CERVANTES, M. L.; CASTILLEJOS, E. Perovskites as catalysts in advanced oxidation processes for wastewater treatment. **Catalysts**, v. 9, 2019.

ROJAS, S.; HORCAJADA, P. Metal-Organic Frameworks for the Removal of Emerging Organic Contaminants in Water. **Chemical Reviews**, v. 120, p. 8378–8415, 2020.

ROYER, S. et al. Perovskites as Substitutes of Noble Metals for Heterogeneous Catalysis : Dream or Reality. **Chemical Reviews**, v. 114, p. 10292–10368, 2014.

SANTHOSH, C. et al. Role of nanomaterials in water treatment applications: A review. **Chemical Engineering Journal**, v. 306, p. 1116–1137, 2016.

SCHOLZ, J. et al. Pore geometry effect on the synthesis of silica supported perovskite oxides. **Journal of Colloid and Interface Science**, v. 504, p. 346–355, 2017.

SHAO, P. et al. Enhanced Activation of Peroxymonosulfate via Sulfate Radicals and Singlet Oxygen by $SrCo_xMn_{1-x}O_3$ Perovskites for the Degradation of Rhodamine B. **Processes**, p. 1–17, 2023.

SOLÍS, R. R.; RIVAS, F. J.; GIMENO, O. Removal of aqueous metazachlor, tembotrione, tritosulfuron and ethofumesate by heterogeneous monopersulfate decomposition on lanthanum-cobalt perovskites. **Applied Catalysis B :Environmental**, v. 200, p. 83–92, 2017.

SOULTATI, A. et al. Synthetic approaches for perovskite thin films and single-crystals. **Energy Advances**, v. 2, p. 1075–1115, 2023.

STEVENS, W. J. J. et al. Investigation of the morphology of the mesoporous SBA-16 and SBA-15 materials. **Journal of Physical Chemistry B**, v. 110, p. 9183–9187, 2006.

SU, W. et al. Activation of peroxymonopulfate by graphene-supported single-atom FeN_5 with an ultra-low dose at low temperature: Nonradical mechanism and antibacterial activity. **Separation and Purification Technology**, v. 330, p. 125657, 2024.

SUKUMAR, M. et al. Co^{2+} substituted $La_2CuO_4/LaCoO_3$ perovskite nanocompoaites: synthesis, properties and heterogeneous catalytic performance. **New Journal of Chemistry**, v. 42, p. 18128–18142, 2018.

THOMAS, N.; DIONYSIOU, D. D.; PILLAI, S. C. Heterogeneous Fenton catalysts: A review of recent advances. **Journal of Hazardous Materials**, v. 404, p. 124082, 2021.

THOMAS, S. et al. Mesoporous metal oxide via nanocasting: Recent advances on types of templates, properties, and catalytic activities. **Materials Today Communications**, v. 40, p. 110152, 2024.

THOMMES, M. et al. Physisorption of gases, with special reference to the evaluation of surface area and pore size distribution (IUPAC Technical Report). **Pure and Applied Chemistry**, v. 87, p. 1051–1069, 2015.

VOORHOEVE, R. J. et al. Perovskite Oxides: Materials Science in Catalysis. **Science**, v. 195, p. 827–833, 1977.

WANG, G. et al. Enhanced degradation of atrazine by nanoscale $LaFe_{1-x}Cu_xO_{3-\delta}$ perovskite activated peroxymonosulfate: Performance and mechanism. **Science of the Total Environment**, v. 673, p. 565–575, 2019.

WANG, N. et al. A review on Fenton-like processes for organic wastewater treatment. **Journal of Environmental Chemical Engineering**, v. 4, p. 762–787, 2016.

WANG, Y. et al. Nanocasted synthesis of mesoporous $LaCoO_3$ perovskite with extremely high surface area and excellent activity in methane combustion. **Journal of Physical Chemistry C**, v. 112, p. 15293–15298, 2008.

WANG, Y. et al. Facet- and defect-dependent activity of perovskites in catalytic evolution of sulfate radicals. **Applied Catalysis B: Environmental**, v. 272, p. 118972, 2020.

WEI, K. et al. Visible-light-driven removal of atrazine by durable hollow core-shell TiO_2@$LaFeO_3$ heterojunction coupling with peroxymonosulfate via enhanced electron-transfer. **Applied Catalysis B: Environmental**, v. 303, p. 120889, 2022.

XIAO, S. et al. Iron-mediated activation of persulfate and peroxymonosulfate in both

homogeneous and heterogeneous ways : A review. **Chemical Engineering Journal**, v. 384, p. 123265, 2020.

XIE, L. et al. Enhanced redox activity and oxygen vacancies of perovskite triggered by copper incorporation for the improvement of electro-Fenton activity. **Chemical Engineering Journal**, v. 428, p. 131352, 2022.

XIONG, Z. et al. Removal of nitrophenols and their derivatives by chemical redox: A review. **Chemical Engineering Journal**, v. 359, p. 13–31, 2019.

XU, P. et al. Use of iron oxide nanomaterials in wastewater treatment: A review. **Science of the Total Environment**, v. 424, p. 1–10, 2012.

YAO, J. et al. Acidic H_2O_2 treatment of $LaCoO_3$ towards highly dispersed Co_3O_4 nanoparticles with excellent catalytic performance for C_3H_8 combustion. **Catalysis Communications**, v. 135, p. 105830, 2020.

YE, T. et al. Efficient Degradation of Rhodamine B Dye through Hand Warmer Heterogeneous Activation of Persulfate. **Sustainability**, v. 15, p. 13004, 2023.

ZHANG, H. et al. Cobalt-doped boosted the peroxymonosulfate activation performance of $LaFeO_3$ perovskite for atrazine degradation. **Chemical Engineering Journal**, v. 452, p. 139427, 2023.

ZHAO, C. et al. Accelerated peroxymonosulfate activation over defective perovskite with anchored cobalt nanoparticles for organic contaminant removal. **Chemical Engineering Journal**, v. 496, p. 153712, 2024.

ZHONG, X. et al. Highly Efficient Copper Doping $LaFeO_3$ Perovskite for Bisphenol A Removal by Activating Peroxymonosulfate. **Catalysts**, v. 13, p. 1–16, 2023.

ZHU, H.; ZHANG, P.; DAI, S. Recent Advances of Lanthanum-Based Perovskite Oxides for Catalysis. **ACS Catalysis**, v. 5, p. 6370–6385, 2015.

ZHU, J. et al. Perovskite Oxides: Preparation, Characterizations, and Applications in Heterogeneous Catalysis. **ACS Catalysis**, v. 4, p. 2917–2940, 2014.

ZITO, P.; SHIPLEY, H. J. Inorganic nano-adsorbents for the removal of heavy metals and arsenic: a review. **RSC Advances**, v. 5, p. 29885–29907, 2015.